

Spring 2019

DYNAMIC MECHANICAL RESPONSE OF ADDITIVELY MANUFACTURED 316L AND AlSi10Mg

Kristofer Kuelper

Follow this and additional works at: https://digitalcommons.mtech.edu/grad_rsch

Part of the [Other Engineering Commons](#)

DYNAMIC MECHANICAL RESPONSE OF ADDITIVELY
MANUFACTURED 316L AND AISi10Mg

by
Kristofer S. Kuelper

A thesis submitted in partial fulfillment of the
requirements for the degree of

Master of Science:
General Engineering

Montana Tech
2019



Abstract

Additive manufacturing (AM), or 3D printing, is a layer by layer method for the fabrication of end use parts. Its utilization in the production of metallic materials, while relatively new, is promising as an alternative technique to build custom or small batch parts with much greater agility than traditional manufacturing methods. The laser powder bed fusion (LPBF) AM technique offers a combination of high geometric accuracy and good mechanical properties for a variety of materials even without post-processing. It can do this by adjusting a number of processing parameters including the intensity of the laser and the thickness of the layers. The characterization of materials produced via LPBF is therefore paramount to the qualification of the process. Charpy v-notch and split Hopkinson pressure bar testing were used to quantify the impact strength of 316L stainless steel and AlSi10Mg aluminum alloys. Samples were produced via LPBF using three different sets of processing parameters for both materials to observe the effects they had on mechanical behavior. The orientation of the build layers, relative to the loading axis of each test, was also varied between 0° and 90° to assess the effect of the inherent anisotropy due to the layer by layer construction. Results for the AlSi10Mg indicated a trend of increasing dynamic compressive strength with the orthogonality of the build layers to the loading axis and a decrease in Charpy absorbed energy from the 0° to 90° build angles. The parameters with the lowest global energy density (GED) showed the highest SHPB flow stress while the medium GED showed the best Charpy absorbed energy. The 316L showed strength trends opposite to those of AlSi10Mg with respect to build angle and little to no variation with processing parameters aside from the low GED Charpy results less which were less than half of the other parameters.

Keywords: Additive Manufacturing, Material Characterization, Split-Hopkinson Pressure Bar, Charpy

Dedication

I would like to thank my parents, Kent and Susie, for their endless love and support as well as my sisters, Kasey and Kortney, for cheering me on throughout this process. This has been a challenging road and they, along with my friends here in Butte, were ever present to instill me with the confidence and encouragement I needed to keep going. Thank you.

Acknowledgements

This work was supported by the Army Research Laboratory and Montana Technological University under Cooperative Agreement [W911NF-15-2-0020]. The views and conclusions contained in this document are those of the authors and should not be interpreted as representing the official policies, either expressed or implied, of the Army Research Laboratory or the U.S. Government. The U.S. Government is authorized to reproduce and distribute reprints for Government purposed notwithstanding any copyright notation herein.

I would like to thank Dr. Brahmananda Pramanik for the opportunity to be a part of his research. Fellow graduate student, Salah Uddin MD, provided valuable insight as he expanded on some of the work performed here. And Riley McNabb was a great help in gathering a significant amount of the data utilized in this work. Collaborations with ARL researcher Brandon McWilliams outside of the primary focus of this work also provided excellent experience and reference material.

Finally, I would like to thank my committee members; Dr. Todd Hoffman, Dr. Sudhakar Vadiraja and Professor Steve Tarrant for valuable advice and taking time out of their schedules to review my work.

Table of Contents

ABSTRACT	II
DEDICATION	III
ACKNOWLEDGEMENTS	IV
LIST OF TABLES.....	VII
LIST OF FIGURES.....	VIII
LIST OF EQUATIONS	XI
GLOSSARY OF ABBREVIATIONS.....	XII
1. INTRODUCTION	1
1.1. Additive Manufacturing	1
1.2. Split-Hopkinson Pressure Bar	2
1.3. Charpy V-Notch	7
1.4. Material Selection	9
1.5. Objective	10
2. EXPERIMENTAL METHODS	11
2.1. Sample Manufacturing.....	11
2.2. Split-Hopkinson Pressure Bar Testing.....	14
2.3. Charpy V-notch Testing	17
3. RESULTS AND DISCUSSION	18
3.1. Aluminum.....	18
3.1.1. SHPB	18
3.1.1.1. Processing Parameter	18
3.1.1.2. Build Angle	22
3.1.2. Charpy V-notch.....	25
3.2. 316L.....	27

3.2.1.	SHPB	27
3.2.1.1.	Processing Parameter	27
3.2.1.2.	Build Angle	32
3.2.1.3.	Temperature	34
3.2.2.	Charpy V-notch.....	35
4.	CONCLUSIONS.....	38
4.1.	<i>AISI10Mg</i>	38
4.2.	<i>316L</i>	38
4.3.	<i>Future Work</i>	39
5.	REFERENCES	40
6.	APPENDIX A: COMPLETE GRAPHICAL DATA.....	45
6.1.	<i>AISI10Mg SHPB Graphs</i>	45
6.2.	<i>AISI10Mg Charpy Graphs</i>	46
6.3.	<i>316L SHPB Graphs</i>	48
6.4.	<i>316L Charpy Graphs</i>	50
7.	APPENDIX B: BACKGROUND CHARPY INFORMATION	52

List of Tables

Table I: AlSi10Mg Feedstock Composition	11
Table II: AlSi10Mg Processing Parameters.....	11
Table III: 316L Feedstock Composition	12
Table IV: 316L Processing Parameters.....	13
Table V: Strain rate and flow stress results for 90° AlSi10Mg specimen	18
Table VI: Strain rate and flow stress results for 0° AlSi10Mg specimen	19
Table VII: Average flow stress at 10% strain for each set of parameters and build orientations	22
Table VIII: Average AlSi10Mg Charpy v-notch absorbed energy results	25
Table IX: Strain rate and flow stress results for 0° oriented 316L.....	28
Table X: Strain rate and flow stress results for 90° oriented 316L.....	28
Table XI: Average flow stress at 10% strain for each set of build parameters and orientations	32
Table XII: Flow stress values for 316L elevated temperature tests.....	34
Table XIII: 316L Charpy v-notch absorbed energy results	35
Table XIV: Low GED AlSi10Mg Charpy Information.....	52
Table XV: Med GED AlSi10Mg Charpy Information	52
Table XVI: High GED AlSi10Mg Charpy Information	53
Table XVII: Low GED 316L Charpy Information	54
Table XVIII: Medium GED 316L Charpy Information	54
Table XIX: High GED 316L Charpy Information.....	55
Table XX: Wrought 316L Charpy Information	55

List of Figures

Figure 1: Laser Powder-Bed Fusion 3D Printing Process [9].....	2
Figure 2: (a) Hopkinson wire testing apparatus. (b) Simplified SHPB setup at Montana Tech.	4
Figure 3: Raw strain data from each pressure bar during an SHPB test.....	5
Figure 4: (a) Standard dimensions for Charpy V-notch specimen (b) Tinius Olsen IT542 Impact Tester [20].....	8
Figure 5: (a) SHPB specimen orientation (b) Charpy v-notch specimen orientation	13
Figure 6: LPBF build platform post feedstock removal. SHPB samples are labeled with build angles.	14
Figure 7: Pressure bar strain data (a) without pulse shaper and (b) with paper pulse shaper	15
Figure 8: Snapshot of an incident pulse and predicted magnitude based on equation (9), pulled from the Sure-Pulse™ analysis software.....	16
Figure 9: Relationship between flow stress and strain rate for (a) 90° and (b) 0° AlSi10Mg samples.....	19
Figure 10: Representative stress strain response of 90° samples at $2.0 \times 10^3/s$ strain rate ..	20
Figure 11: Average flow stress of samples from each set of processing parameters for (a) 90° and (b) 0° build orientations	21
Figure 12: Average flow stress for each set of processing parameters across all build orientations	23
Figure 13: Comparison of a 0° specimen tested at $2.5 \times 10^3 /s$ strain rate (left) and an untested specimen (right)	24

Figure 14: Circumferential fracture surface of an AlSi10Mg SHPB sample from (a) the present study and from (b) a similar study [32]	24
Figure 15: Average absorbed energy of aluminum Charpy v-notch specimen (*only two specimens available for testing).....	26
Figure 16: Relationship between flow stress and strain rate for (a) 0° and (b) 90° 316L samples	29
Figure 17: Representative stress strain response of 316L samples at $1.5 \times 10^3/s$ strain rate	30
Figure 18: Average flow stress of samples from each set of processing parameters for (a) 0° and (b) 90° build orientations	31
Figure 19: Average flow stress for each set of processing parameters across all build orientations	33
Figure 20: Average absorbed energy of stainless steel Charpy v-notch specimen.....	35
Figure 21: Fracture surface comparison between high and low GED Charpy specimen ..	36
Figure 22: Average flow stress of low GED AlSi10Mg (error bars represent standard deviation)	45
Figure 23: Average flow stress of medium GED AlSi10Mg (error bars represent standard deviation)	45
Figure 24: Average flow stress of high GED AlSi10Mg (error bars represent standard deviation)	46
Figure 25: Average absorbed energy of low GED AlSi10Mg Charpy v-notch specimen (error bars represent standard deviation)	46
Figure 26: Average absorbed energy of medium GED AlSi10Mg Charpy v-notch specimen (error bars represent standard deviation)	47

Figure 27: Average absorbed energy of high GED AlSi10Mg Charpy v-notch specimen (error bars represent standard deviation)47

Figure 28: Average flow stress of Low GED 316L (error bars represent standard deviation)48

Figure 29: Average flow stress of medium GED 316L (error bars represent standard deviation)48

Figure 30: Average flow stress of high GED 316L (error bars represent standard deviation)49

Figure 31: Stress Strain response of High GED 316L at elevated temperatures49

Figure 32: Average absorbed energy of low GED 316L Charpy v-notch specimen (error bars represent standard deviation)50

Figure 33: Average flow stress of high GED 316L (error bars represent standard deviation)50

Figure 34: Average flow stress of high GED 316L (error bars represent standard deviation)51

List of Equations

Equation_(1)	5
Equation_(2)	5
Equation_(3)	6
Equation_(4)	6
Equation_(5)	6
Equation_(6)	6
Equation_(7)	8
Equation_(8)	12
Equation_(9)	16
Equation_(10)	34

Glossary of Abbreviations

Term	Definition
AM	Additive Manufacture
SLM	Selective Laser Melting
LPBF	Laser Powder Bed Fusion
SHPB	Split-Hopkinson Pressure Bar
ASTM	American Society for Testing and Materials
GED	Global Energy Density
EOS	Electro Optical Systems™

1. Introduction

1.1. Additive Manufacturing

Additive manufacturing (AM), or 3D printing as it is better known, is a relatively new means of producing end use parts. While somewhat ubiquitous as a method for polymer-based structures, the application for metals is still being refined and characterized. The process is based on layer-by-layer construction of parts using a concentrated heat source to melt the feedstock, wire or powder, into cross sectional planes perpendicular to the build direction. As the top layer cools it adheres to the previous layers forming a solid, singular part [1]. Recent advancements have allowed for quicker and less wasteful production and greater complexity than traditional manufacturing methods like casting or machining can achieve [2], [3]. Its inherent agility makes it especially useful on smaller scales where lead times and economy for specialized and custom parts can be vastly reduced. These advantages are making AM a significant target for research effort as it holds industry changing potential for in situ production as well as increased design efficiency through topology optimization [4]. Interested industries range from the military, for the ability to produce parts on demand, to the medical industry to economically build custom, highly geometrically complex devices [5].

An effective way to categorize AM processes is by the method of feed stock delivery. The majority of mainstream AM practices fall into powder bed, powder feed and wire feed systems. The largest differences between them are the geometric accuracy and deposition rate of material. Powder bed/feed systems can attain quite impressive resolution, 0.025 mm for powder-feed [6] and 0.04 mm for powder-bed, but offer low deposition rates. Wire feed processes can achieve much higher deposition rates, but only by sacrificing dimensional accuracy (about 10 times lower than powder systems) [7]. Powder bed processes use a laser or electron beam to melt

part cross sections on a pre-laid sheet of metallic powder before another layer of powder is evenly raked across the work bed as shown in Figure 1. This process continues until a three-dimensional part is constructed. Due to the usability of near as-built parts and its current dominance in metallic 3D printing [8], a method called laser powder-bed fusion (LBPF) printing, was chosen to fabricate the test specimen.

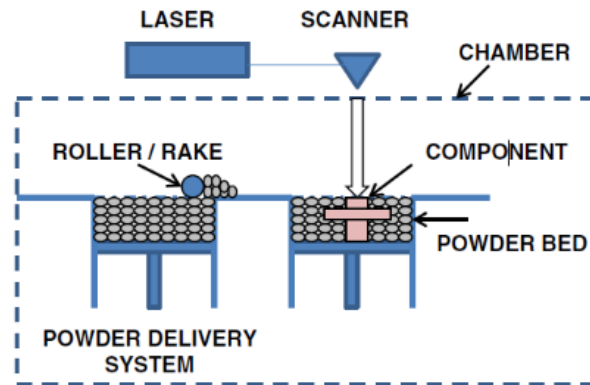


Figure 1: Laser Powder-Bed Fusion 3D Printing Process [9]

Materials produced through AM processes have some inherent differences from traditionally manufactured. Due to the nature of the cyclic melting and solidification that create unique thermal histories at each layer, there are boundaries between them that cause a degree of anisotropy, even under ideal conditions [1]. The complexity of the AM process also lends itself to considerable variation by alteration of the processing parameters, especially input power and scanning speed [10]. Therefore, the importance of characterizing the process and the products of AM is paramount.

1.2. Split-Hopkinson Pressure Bar

High strain-rate testing is necessary for establishing material behavior under certain impact loading conditions as it differs from quasi-static performance, which is more traditionally used as a strength metric. Split-Hopkinson pressure bar (SHPB) testing offers a method for

inducing controlled high rate loading and recording material response in the form of stress, strain and strain-rate [11].

The split-Hopkinson pressure bar test, also known as the Kolsky bar test, was invented in its original form by John Hopkinson in 1872 [11]. It was intended to study the rupture behavior of iron wires due to attached falling weights, but it also demonstrated the propagation of stress waves. Bertram Hopkinson later used horizontal rods to attempt to measure the pressure induced by a gunshot impact, but the technology at the time was too primitive to accurately measure the event. In the late 1940s Davies proposed new mathematical models for the wave propagation [12] using condensers to track deformation due to the stress waves. Herbert Kolsky improved upon the design and Hopkinson's theory by creating a horizontal compression-based setup, which used two pressure bars in series with a sample and a controlled explosion to induce high strain rates in the sample. This new method allowed for significant increase in the accuracy and controllability of the experiments and was able to create stress-strain data for the sample specimen [13]. Following Kolsky's design Krafft was the first to produce significant data with the setup in the early 1950s [14]. As a result, the Kolsky bar or split-Hopkinson pressure bar setup looks drastically different from the original Hopkinson experiment, as shown in Figure 2.

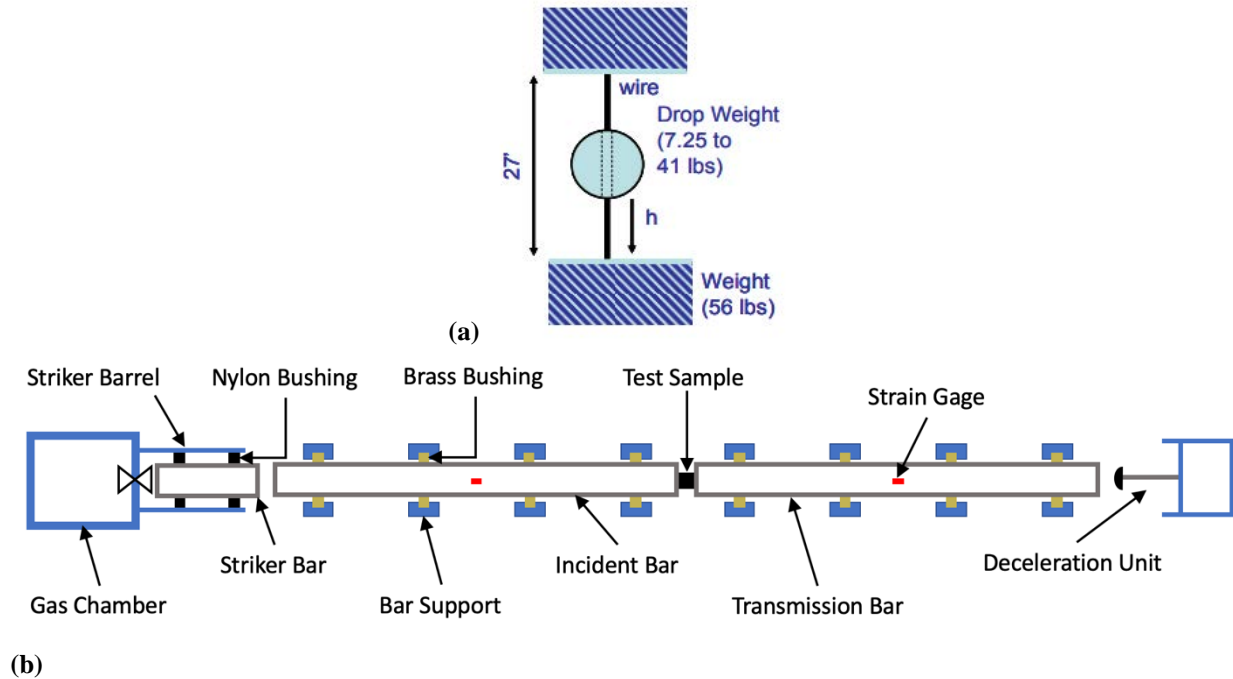


Figure 2: (a) Hopkinson wire testing apparatus. (b) Simplified SHPB setup at Montana Tech.

The modern SHPB setup is similar to the original Kolsky with a few notable changes. For the external impact source, the explosion was replaced with a striker bar of identical material and diameter as the incident and transmission bar. The striker is centered with nylon bushings, to ensure a flush interface with the incident bar, and launched by a compressed gas gun to improve consistency between tests. The incident and transmission bars ride on precision machined bushings or bearings for near frictionless translation, and strain gages mounted on each are used to measure the magnitude of the strain waves much more accurately [15].

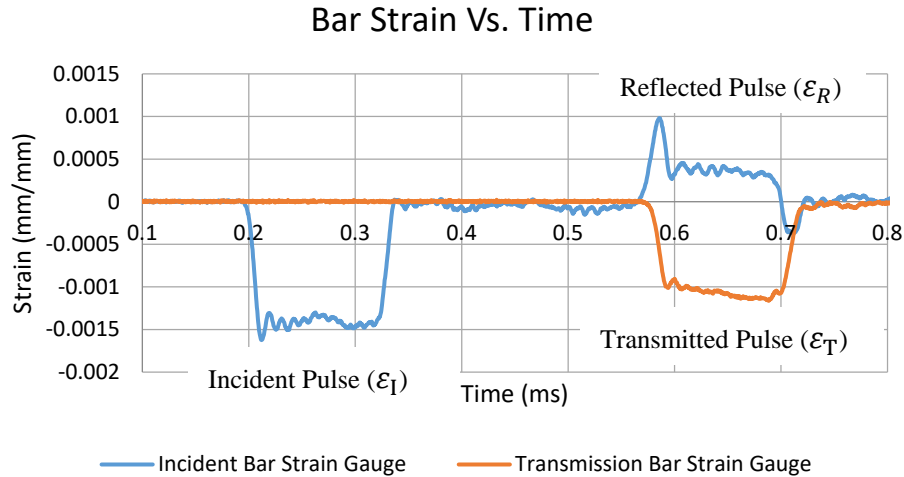


Figure 3: Raw strain data from each pressure bar during an SHPB test

Data from the strain gages is passed through a signal conditioning amplifier and recorded on a connected computer. The raw data is then processed for several key parameters through equations 1-3 [11], [16]. The initial incident stress pulse represents the energy input due to striker impact. The reflected stress wave is created due to the impedance mismatch between the incident bar and specimen. From that pulse, the strain rate imparted on the sample is derived by equation (1).

$$\dot{\varepsilon}(t) = -\frac{2(C_b)\varepsilon_R(t)}{L_0} \quad (1)$$

where C_b is the speed of sound in the incident bar, L_0 is the initial length of the specimen and ε_R is the strain magnitude of the reflected wave on the bar.

The strain at each point can be then determined by the integration of the strain rate over time as shown in equation (2).

$$\varepsilon(t) = \int_0^t \dot{\varepsilon}(\tau) d\tau = -\frac{2C_b}{L_0} \int_0^t \varepsilon_R(\tau) d\tau \quad (2)$$

where t is the moment of interest or the total duration of loading and τ represents time.

Another portion of the stress wave passes into the specimen and again splits at the transmission face of the sample with some passing through to the transmission bar and the rest reverberating within the sample itself. The reverberation helps distribute the stress equally throughout the specimen and is analyzed to ensure uniform stress (approximately three reflections) before the transmission pulse ends or before the specimen completely fails. Stress during the impact, also referred to as flow stress due to the exclusively plastic deformation occurring, is determined from the transmitted pulse by equation (3).

$$\sigma(t) = \frac{E_b A_b \varepsilon_T(t)}{A_s} \quad (3)$$

where E_b is the elastic modulus of the bar, A_b and A_s are the cross-sectional areas of the bar and specimen respectively and ε_T is the strain magnitude of the transmitted wave.

Due to the excessive strains achievable through the SHPB method, engineering stress and strain will provide somewhat misleading data as the cross section of the specimen expands and the length diminishes. This can lead to overestimating the stress increase under deformation and the appearance of fading strain rate. To compensate, the data will be converted from engineering stress and strain to true stress and strain by way of equations (4), (5) and (6) [17].

$$\varepsilon_t(t) = -\ln(1 - \varepsilon(t)) \quad (4)$$

$$\dot{\varepsilon}_t(t) = \frac{\dot{\varepsilon}(t)}{1 - \varepsilon(t)} \quad (5)$$

$$\sigma_t(t) = (1 - \varepsilon(t))\sigma(t) \quad (6)$$

where all variables with the subscript “*t*” are true values and all variable without subscripts are engineering values as determined in equations (1), (2) and (3).

The SHPB testing performed in this work will focus on the compressive behavior of additively manufactured 316L stainless steel and AlSi10Mg aluminum. The strain rates ranged

from 500/s to 3000/s under conditions from ambient room temperature to 300°C. Elevated temperatures were achieved with the use of an infra-red sleeve heater. The experimental results are represented in graphical form and as average values of stress, strain and strain-rate, which will be used to quantify and compare impact strength.

1.3. Charpy V-Notch

The Charpy, or Charpy v-notch test, is a pendulum-based impact test. It was proposed by S.B. Russell in 1898 and as well by G. Charpy in 1901, although Charpy's later contribution to the creation of specific test procedures and data collection led it being named for him [18]. By 1914 the procedure and equipment designated for the testing closely resembled what is used today. In 1933 the first ASTM standard for Charpy testing, ASTM E23, was released and is still the standard, subjected to yearly review [19].

The primary focus of Charpy testing is the fracture toughness of the materials. This is determined by measuring the potential energy of the pendulum after it completely fractures the specimen and subtracting that from the known initial potential energy. The notched bar is set across two anvils with the notch facing away from the hammer. The hammer, an 8-mm radial impact surface, is suspended on the end of the pendulum. The notch is added to the otherwise smooth surface at the center of the specimen to control the fracture growth and location by creating a high stress concentration at that point. A schematic of a standard Charpy V-notch sample and a Charpy tester are shown in Figure 4.

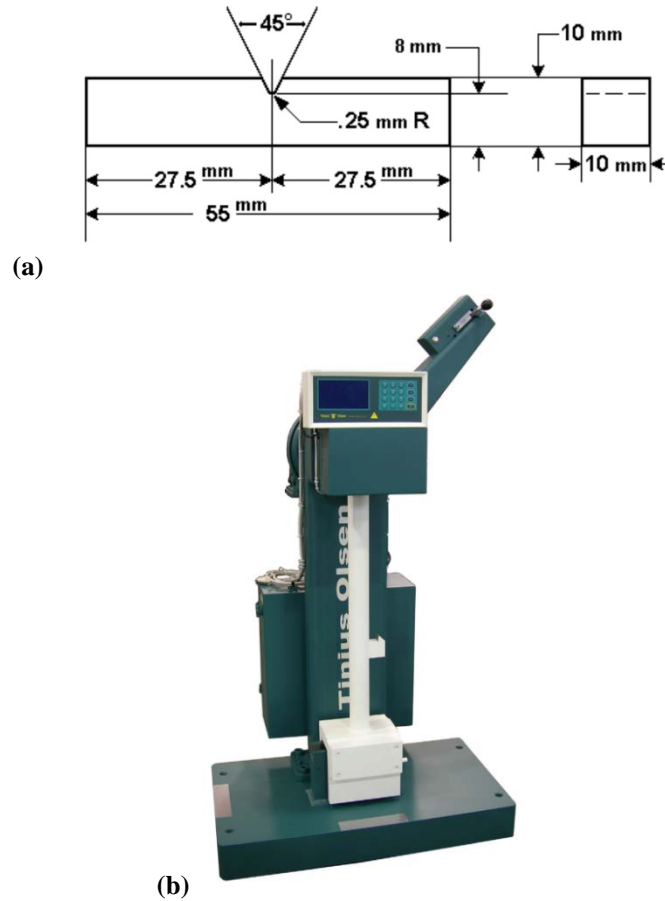


Figure 4: (a) Standard dimensions for Charpy V-notch specimen (b) Tinius Olsen IT542 Impact Tester [20]

When the test is begun, the pendulum swings from a known height with a known potential energy, breaks the specimen by causing a fracture to propagate from the notch all the way through the specimen. The maximum potential energy of the pendulum after the impact is measured and subtracted from the initial potential energy, shown in equation (7), giving the energy absorbed by the sample during fracture [21].

$$E_a = mg(h_0 - h_f) \quad (7)$$

where m is the pendulum mass, g is the gravitational constant and h_0 and h_f represent the height of the pendulum before release and at peak height after fracturing the specimen.

1.4. Material Selection

Aluminum and stainless steel were both selected for their significant utilization as engineering materials. Aluminum represents the second most used metal behind steel [22], applications range widely due to its low density, high heat conductivity and corrosion resistance. Stainless steel boasts excellent biocompatibility [23] and shares aluminum's favorable corrosion resistance, but is very robust and a better option when size and cost are more important than weight. The alloys chosen, 316L and AlSi10Mg, also possess characteristics that make them excellent candidates for LPBF fabrication.

The weldability of 316L stainless steel is excellent owing to its low carbon and moderate molybdenum content, which translates well to the SLM process [24]. Its resistance to hot and cold cracking helps it withstand the repeated melting, solidification and extreme temperature gradients. Considerable work has also been done to increase the build rates and optimize processing parameters to achieve nearly fully dense (>99%) bulk material with some properties meeting or exceeding those of traditionally manufactured steel [25].

Similarly, AlSi10Mg has good weldable characteristics [26] and is very well adaptable to the LPBF process. The rapid cooling experienced solidification of each layer lends itself to the formation of very fine microstructures [27], combined with the static positioning of the raw material, LPBF can achieve superior homogeneous feature distribution when compared to casting processes [28]. This allows as-built LPBF AlSi10Mg to achieve strengths similar or better to T6 treated cast aluminum [29], [30] without post production treatment. This alloy has also been the subject of considerable research and can be produced at close to 100% density via SLM methods [26], [28], [29]. The mechanical properties of aluminum have been shown to rely considerably on the processing parameters when SLM is used [31] and therefore SHPB can

likely provide valuable data on processing parameter effects on dynamic behavior which has been relatively under explored [32].

1.5. Objective

Robust characterization of engineering materials is vital to their effective application and widespread adoption. This work in concert with other research being performed at Montana Tech [24], [33]–[35], seeks to establish the physical and mechanical properties of several additively manufactured metals under a wide range of conditions. The metals, AlSi10Mg aluminum and 316L stainless steel, will be tested via the Charpy v-notch and SHPB methods to establish their resistance to fracture and compressive strength respectively, under high-rate loading conditions. Specimen for both methods will be prepared via LPBF under several production parameters. These parameters will include variance in the global energy density (GED) and build orientation. Charpy v-notch testing will be performed in accordance with ASTM E-23 and although there is no ASTM standard for SHPB, testing will be performed in accordance with common best practices found in other research and as laid out in the ASM handbook [36]. Charpy v-notch testing will be performed at ambient temperature to establish its performance relative to traditionally manufactured, wrought material. SHPB experimentation will incorporate high temperatures, up to 300°C via an infra-red chamber heating sleeve, in addition to covering strain rates between 1000/s and 2000/s. This testing regime should be able to identify the dependence of high strain rate response on the processing parameters and orientation of the material within the build volume. It should serve as a foundation for future work in optimizing AM techniques and modeling the high strain rate behavior.

2. Experimental Methods

2.1. Sample Manufacturing

The AM samples were all produced by a third-party manufacturer using the Electro Optical Systems M290 industrial 3D printer. The CAD files for all required specimen were provided to the manufacturer and all slicing and support structure additions were performed by them in accordance with industry standards.

The aluminum powder used to produce the AlSi10Mg samples was sourced from the printer manufacturer, Electro Optical Systems (EOS). The nominal particle size of the powder was 20 μ m and the composition was as shown in Table I.

Table I: AlSi10Mg Feedstock Composition

Material	Wt. Percent
Al	Balance
Si	9.0-11.0
Fe	≤ 0.55
Cu	≤ 0.05
Mn	≤ 0.45
Mg	0.2-0.45
Ni	≤ 0.05
Zn	≤ 0.10
Pb	≤ 0.05
Sn	≤ 0.05
Ti	≤ 0.15

The aluminum samples were produced by the EOS M 290 printer using three different sets of processing parameters. The primary parameters are listed in Table II, all others were set according to industry standards and best practices set out by EOS.

Table II: AlSi10Mg Processing Parameters

Parameter	Low GED	Med GED (P)	High GED
Hatch Spacing (mm)	0.209	0.209	0.19
Scanning Speed (mm/s)	1430	1170	1300
Laser Power (W)	333	333	370
Layer Thickness (mm)	0.03	0.03	0.03
Energy Density (J/mm³)	37.1	45.4	49.9

The energy density is a resultant value for a set of processing parameters that indicated the amount of energy per unit volume used to melt the feedstock. It is calculated using the formula in equation (8) [37].

$$\Psi = \frac{P}{v * h * t} \quad (8)$$

where P is the laser power in watts, v is the laser scanning speed in mm/s, h is the hatch spacing in mm and t is the layer thickness in mm.

The printed samples were then machined to the proper specimen dimensions with a high degree of precision. There was no other post-processing done on the specimen such as annealing or heat treatment.

Stainless steel samples were similarly produced, by a third party using the EOS M 290 3D printer with EOS supplied 316L powdered stainless steel feedstock. The composition of the feedstock was as shown in Table III.

Table III: 316L Feedstock Composition

Material	Wt. Percent
Fe	Balance
Cr	16.9
Ni	12.1
Mo	2.4
C	≤0.030
Mn	≤2.00
Cu	≤0.50
P	≤0.025
S	≤0.010
Si	≤0.75
N	≤0.10

The stainless steel samples were produced using three different sets of processing parameters yielding three unique energy densities. Table IV shows the values for the energy densities of each and the effecting parameters.

Table IV: 316L Processing Parameters

Parameter	Low GED	Med GED	High GED
Hatch Spacing (mm)	0.108	0.09	0.072
Scanning Speed (mm/s)	1300	1083	866
Laser Power (W)	234	195	234
Layer Thickness (mm)	0.02	0.02	0.02
Energy Density (J/mm^3)	83.3	100.	188

Following the extraction of the samples from the powder bed, they were machined to a high degree of dimensional accuracy and were tested without any other post processing.

Aluminum and stainless steel samples were also produced with varying build orientations to examine the effect of the inherent anisotropy of the additive manufacturing process without post heat treatment. The orientations were 0° , 30° , 45° , 60° and 90° . For SHPB tests, the angles represent layer variation from the loading axis and for Charpy the angles represent build layer variation from the length wise axis of the specimen as shown in Figure 5. Another view is available in Figure 6

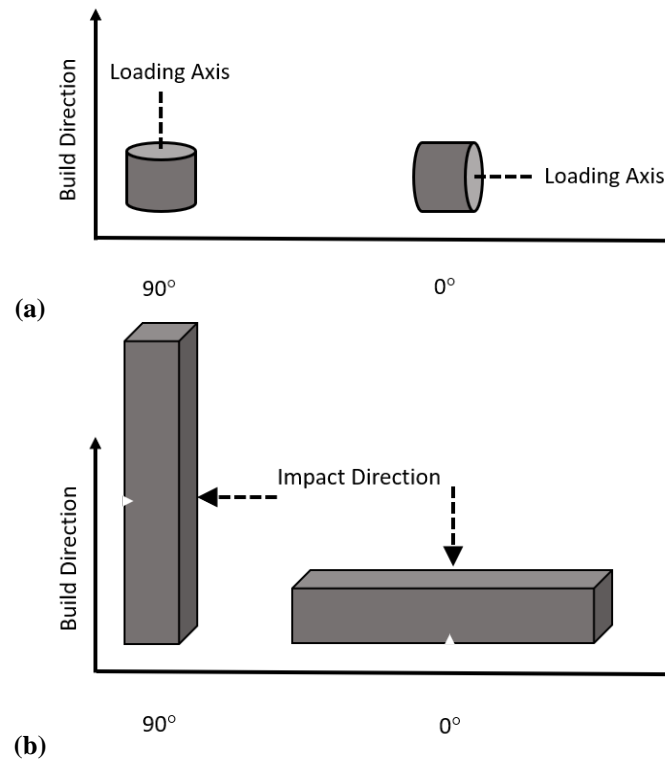


Figure 5: (a) SHPB specimen orientation (b) Charpy v-notch specimen orientation

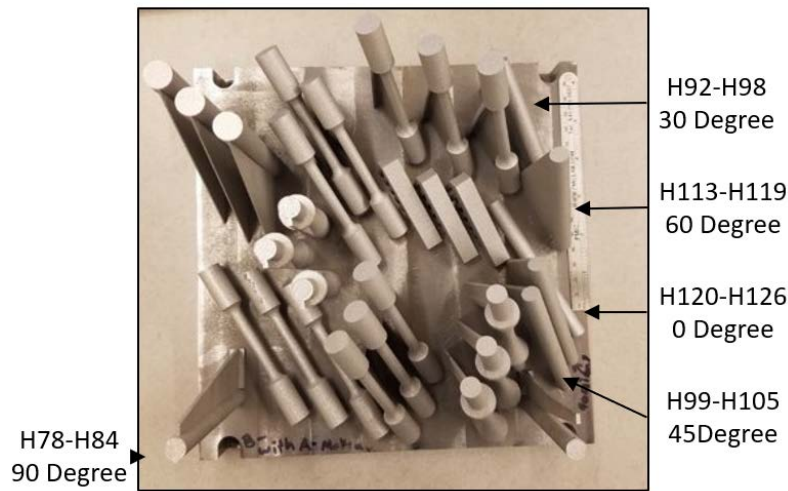


Figure 6: LPBF build platform post feedstock removal. SHPB samples are labeled with build angles.

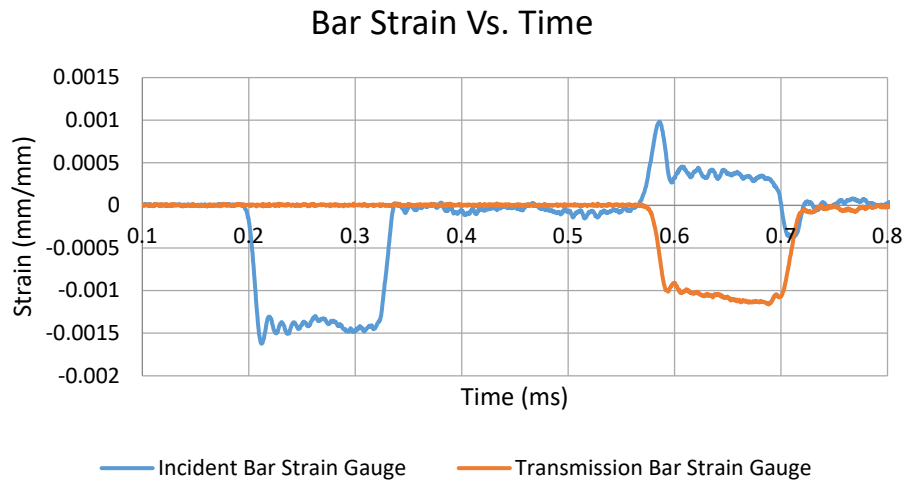
2.2. Split-Hopkinson Pressure Bar Testing

The SHPB testing was performed on an REL Split-Hopkinson pressure bar/Kolsky bar assembly. Identical setups were used to test the aluminum and the stainless steel samples although some parameters, specifically impact velocity, were varied to account for the differing strain rate responses of the materials. The pressure bars utilized were C350 maraging steel bars 72 inches in length and 0.75 inches in diameter. For all tests the striker bar was 12 inches in length by 0.75 inches in diameter and made of C350 maraging steel to ensure impedance match with the incident bar.

A gas gun was used to accelerate the striker bar to the desired velocity for each test. Consistency was maintained by computer-controlled charge and release valves. An adjustable barrel ensured alignment and a flush connection between the striker and incident bar for reliable and desirable pulse shapes. In addition, a paper pulse shaper was used between the striker and incident bar to reduce the “ringing” effect shown in Figure 7 and increase pulse rise times, thereby lowering the strain at specimen equilibrium. At the opposite end of the bars was a high-

pressure pneumatic damper to decelerate the transmission bar during post event translation due to the reflection of the transmitted wave at the far end of the bar opposite the specimen.

(a)



(b)

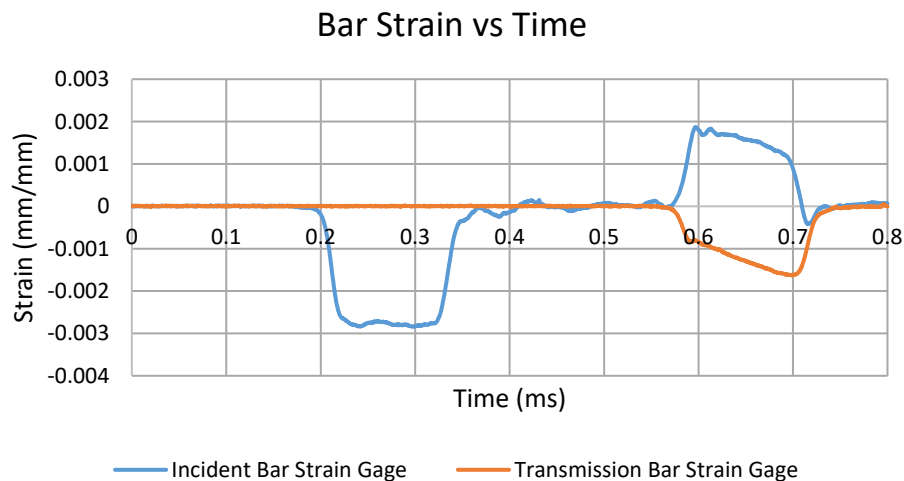


Figure 7: Pressure bar strain data (a) without pulse shaper and (b) with paper pulse shaper

Measurement of the pulses traveling in the pressure bars was determined with 120Ω linear strain gages wired through a Vishay 2310B signal conditioning amplifier with a quarter-bridge circuit configuration. A digital oscilloscope received the signal and transmitted it to a

computer capable of recording the event with a bit depth of 15 at 8 ns sampling intervals for both incident and transmitted channels.

Calibration of the accuracy of strain measurements was performed periodically. The process for calibration is fairly simple as the magnitude of the incident pulse can be easily and accurately predicted by equation (9).

$$\varepsilon_I = \frac{V}{2C_b} \quad (9)$$

where ε_I is the magnitude of the incident pulse plateau, V is the impact velocity of the impedance matched striker bar and C_b is the speed of sound within the pressure bar. A typical incident pulse with predicted magnitude is highlighted in Figure 8.

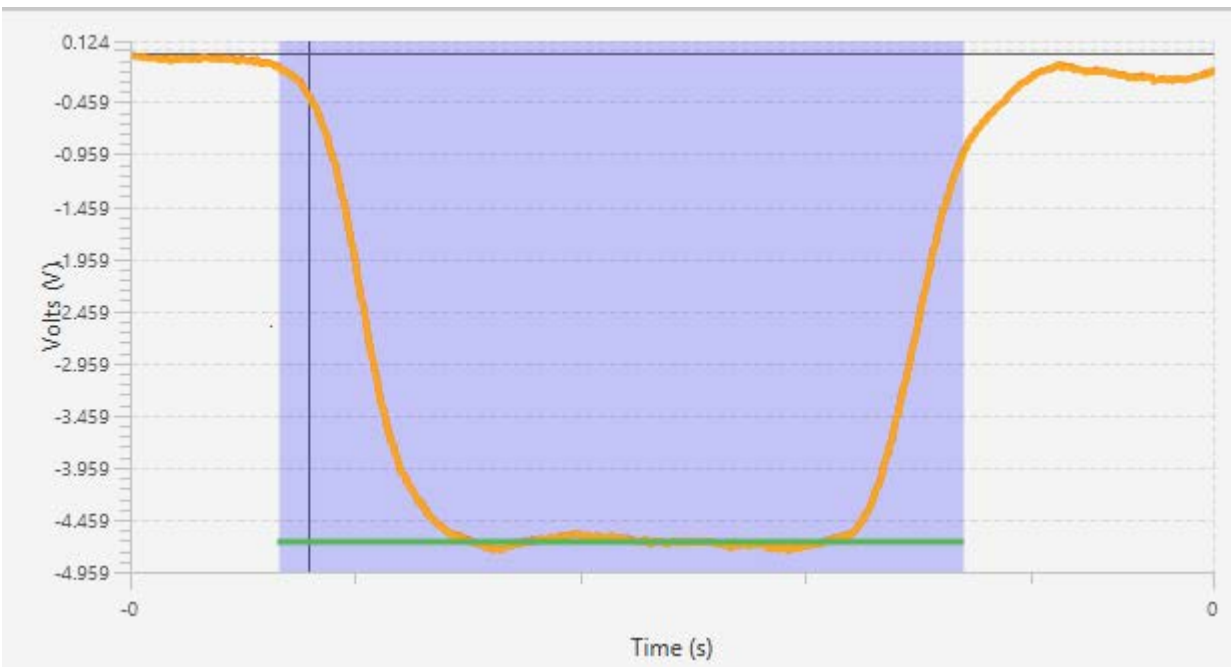


Figure 8: Snapshot of an incident pulse and predicted magnitude based on equation (9), pulled from the Sure-Pulse™ analysis software.

Temperature increases were done on several 316L specimen tests and were achieved using a 4 kW infra-red heating sleeve. The clamshell sleeve locked concentrically around the specimen with some of the heating length covering the pressure bar ends. Temperatures were

measured with a K-type thermocouple inserted into a sacrificial sample and monitored during several calibration heating runs. The rise times for each target temperature were averaged for the actual tests. To maintain the viscoelastic properties of the pressure bars, the temperature was maintained below 400°C and heating times were kept to a minimum while still accounting for a drop between removing the sleeve and firing the striker (approximately 2 seconds).

2.3. Charpy V-notch Testing

Charpy v-notch testing was performed on a Tinius Olsen model IT542 with a pendulum energy of 542J. All tests were performed at ambient temperature (approximately 20°C) for a baseline comparison of the material variations. All variations were tested three times to get an average value for absorbed energy.

3. Results and Discussion

3.1. Aluminum

3.1.1. SHPB

The results for split-Hopkinson pressure bar testing will be presented both graphically and numerically. Due to the number of plots, the graphs will not include stress strain plots from every trial. All plots not included in this section will be available in Appendix A: Complete Graphical Data. Discrete flow stress values presented in tables or bar charts are the instantaneous flow stress value samples at 10% strain during each event unless otherwise noted. This is done to make the values independent of strain hardening and to avoid data from the unstable loading period.

3.1.1.1. Processing Parameter

The first comparison is between the three different processing parameters sets. The values of the primary variables for each build are listed in Table II.

True flow stress and true strain rate values for tests of the 0° and 90° build angles are shown in Table V and Table VI and Figure 9.

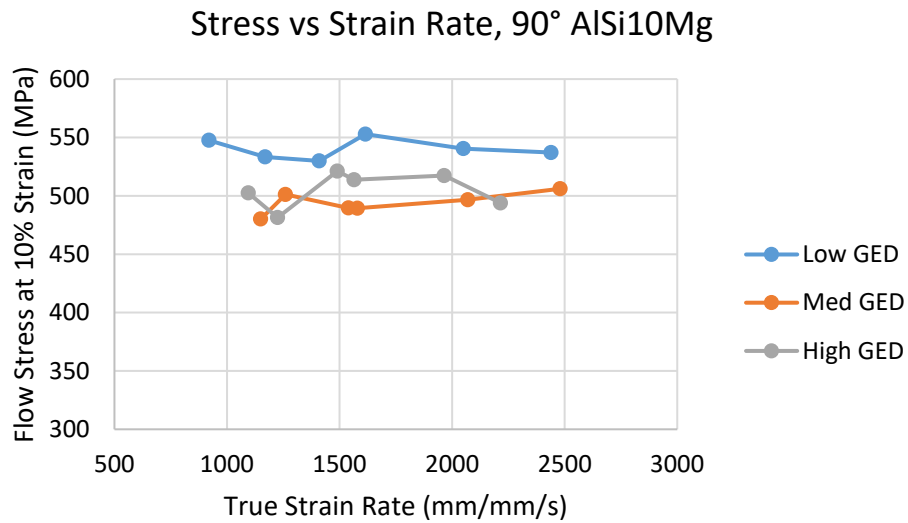
Table V: Strain rate and flow stress results for 90° AlSi10Mg specimen

Low GED		Med GED		High GED	
Strain Rate	Flow Stress	Strain Rate	Flow Stress	Strain Rate	Flow Stress
920	548	1150	480	1095	502
1170	533	1260	501	1225	481
1410	530	1540	490	1490	521
1615	553	1580	489	1565	514
2050	540	2070	497	1965	517
2440	537	2480	506	2215	494

Table VI: Strain rate and flow stress results for 0° AlSi10Mg specimen

Low GED		Med GED		High GED	
Strain Rate	Flow Stress	Strain Rate	Flow Stress	Strain Rate	Flow Stress
1280	483	1300	470	900	472
1290	486	1335	513	990	471
1460	473	1370	462	1630	463
1670	488	1765	466	1660	460
2400	482	2365	476	2150	459
2600	494	2490	475	2450	471

(a)



(b)

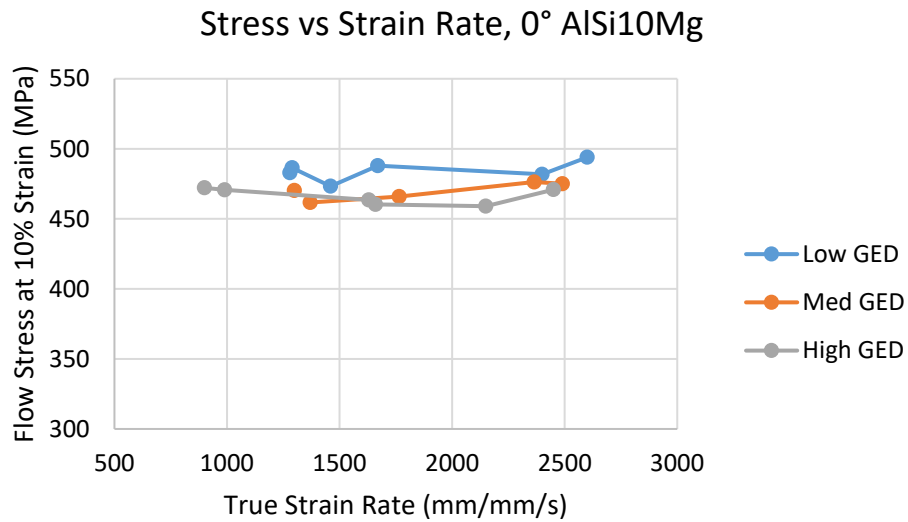


Figure 9: Relationship between flow stress and strain rate for (a) 90° and (b) 0° AlSi10Mg samples

Strain rates achieved for the 90° AlSi10Mg samples largely ranged from around 1000/s to around 2500/s. Within this range there is not a discernable or statistically significant trend in flow stress with respect to strain rate. This aligns with other SHPB experimentation done on the AM AlSi10Mg alloy which could find no strain rate sensitivity in the high-strain rate range (10^2 /s to 10^4 /s) [32].

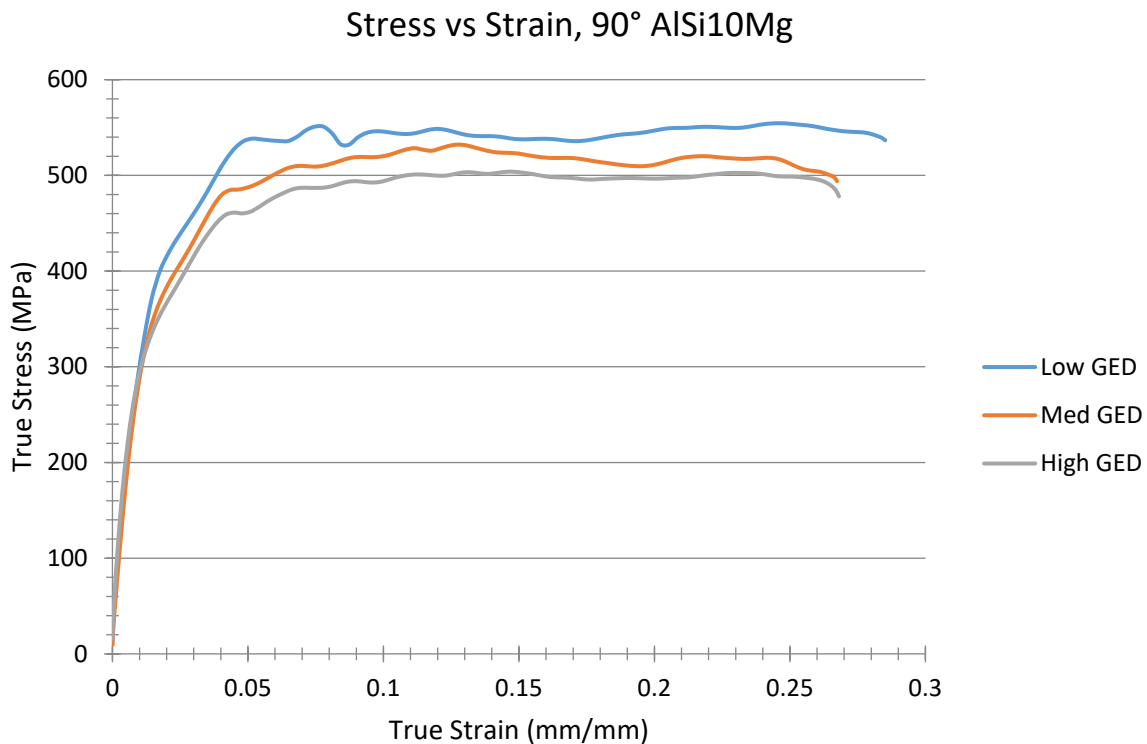


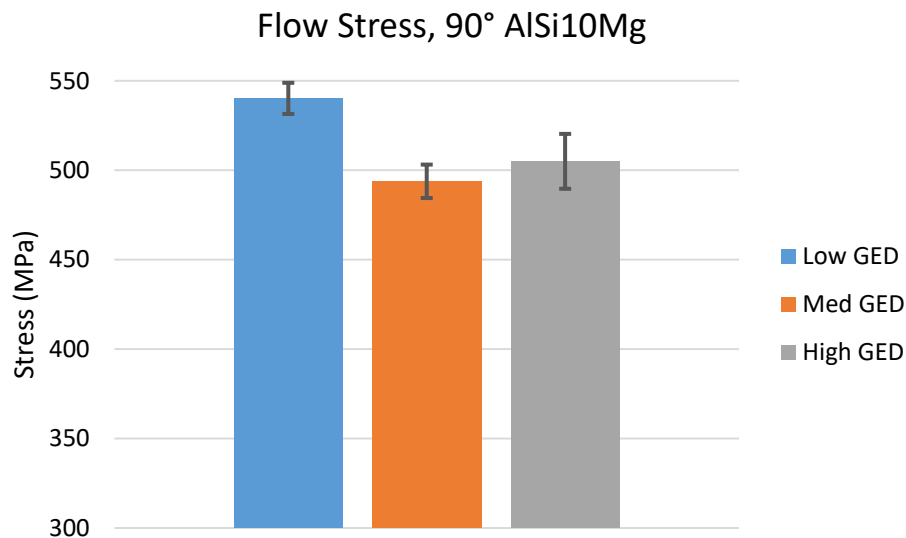
Figure 10: Representative stress strain response of 90° samples at 2.0×10^3 /s strain rate

A representative sample from each set, chosen for clarity, is shown in Figure 10. Plotted there are the stress strain responses of AlSi10Mg samples with a 90° build angle. The maximum variation between samples of different parameters is between the highest and lowest GEDs with the middle GED falling between the two, as would be expected if the GED was directly related to material performance. The plateau in the stress strain response despite significant deformation also demonstrates a distinct absence of strain sensitivity or work hardening above 5%

deformation at this strain rate. This is generally caused by dominance of thermal softening over the typical strain hardening seen in quasi static testing [11].

The flow stress at 10% strain was found for each individual test and averaged amongst samples with identical build angles and parameters, and of varying strain rates. Figure 11 presents these averages visually.

(a)



(b)

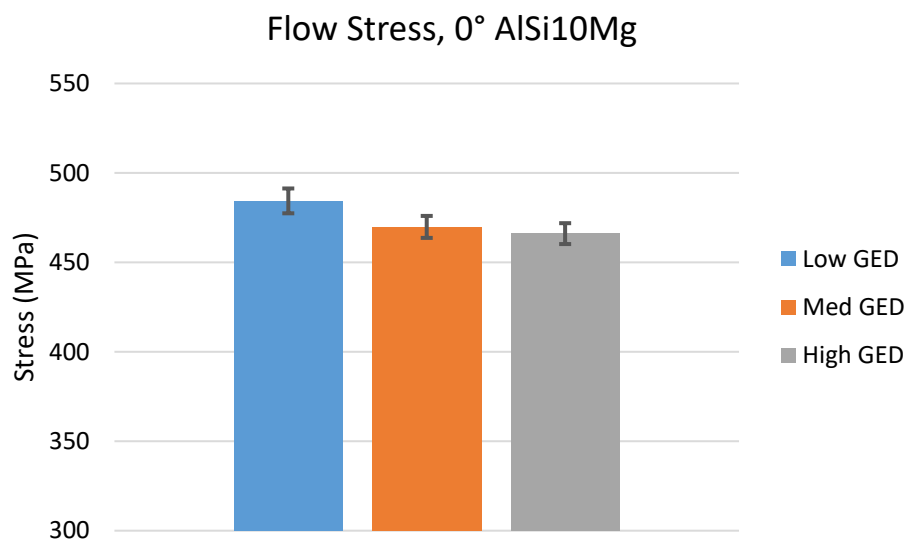


Figure 11: Average flow stress of samples from each set of processing parameters for (a) 90° and (b) 0° build orientations

The error bars on each average represent the standard deviation of the sample set of six. For samples built in the 90° orientation, although the increase in flow stress is only around 9%, the consistency of the results indicates a statistically significant advantage in dynamic compressive strength with the lower GED parameters over the medium or high GED parameters. For samples produced in the 0° orientation, the flow stress advantage of the low GED parameters is reduced to around 3% and very close to overlapping the first standard deviation ranges. This indicates the presence of deformation mechanisms that have varying dominance based on the orientation of the build layers relative to loading.

3.1.1.2. Build Angle

Strength variation due to the orientation of build layers is represented in Table VII as the average of each sample set where the uncertainties represent standard deviation. Test samples for 30° high GED parameters were unavailable due to print failure during manufacture.

Table VII: Average flow stress at 10% strain for each set of parameters and build orientations

	Low GED	Med GED	High GED
Build Angle	Flow Stress (MPa)	Flow Stress (MPa)	Flow Stress (MPa)
0 Degree	484 ± 6.94	470 ± 6.14	466 ± 5.84
30 Degree	501 ± 3.48	479 ± 8.45	(No Data)
45 Degree	510 ± 6.08	494 ± 4.04	492 ± 6.35
60 Degree	520 ± 8.49	494 ± 6.37	505 ± 13.67
90 Degree	540 ± 8.71	494 ± 9.35	505 ± 15.34

There doesn't appear to be a consistent trend in the uncertainty with respect to build angle or build parameter although the largest standard deviations are from the high GED parameters at 60° and 90°. These deviations are significantly larger than those of other sample sets and could signal a slight reduction in the ability to control the consistency of the product using these parameters. Despite that the maximum coefficient of variation is only 3%, with most sample sets being between 1-2%. This adds significance to the trends observed even with the small variations between build angle and GED.

Visual representation of the flow stress data with respect to build angle and processing parameters is given in Figure 12.

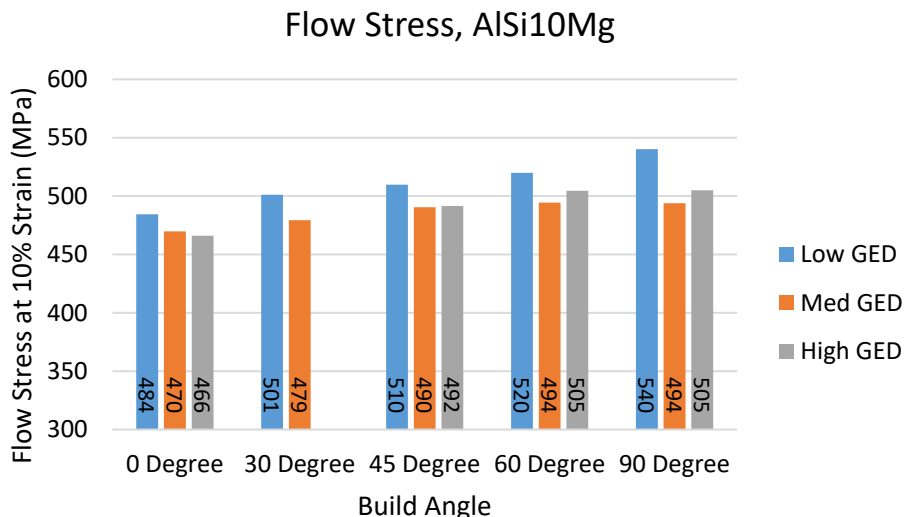


Figure 12: Average flow stress for each set of processing parameters across all build orientations

The most apparent feature is the prominence of the low GED parameters over the medium and high GEDs. The difference is noticeable at all build angles although it is greatest at the 90° orientation. This advantage could be due to the higher scanning speed, lower laser power and therefore higher cooling rates of the low GED parameters. Increased cooling rates tend to create finer microstructure capable of withstanding higher stresses under plastic deformation [27].

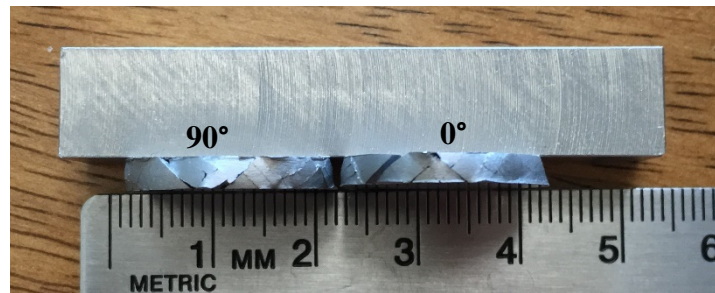
The increase in strength with the increase perpendicularity of build angle to compression loading axis in AM aluminum has been noted elsewhere for this strain rate range [32]. The 90° orientation places the weaker planes between build layers in compression, whereas other angles subject those planes to enhanced shear and tension. This can increase the effect of ASB and increase the likelihood of delamination. The most apparent result of that is the elliptical shape that non-90° specimen take on after large deformations as shown in Figure 13.



Figure 13: Comparison of a 0° specimen tested at 2.5×10^3 /s strain rate (left) and an untested specimen (right)

Posttest analysis of fractured AlSi10Mg specimen in other work indicates a dominant brittle failure mechanism for as-built samples [32]. Given the size of specimens used in the present study, observable failure was not achieved during standard SHPB testing, although direct striker to specimen impact was able to cause significant failure. End-to-end cracks at 45° to the loading axis and relatively featureless, smooth fracture surface could be seen on samples tested here and in the previous study, as shown in Figure 14. Some variation in the radial deformation of the samples can be noted although its significance is questionable based on the method used in achieving these failures.

(a)



(b)

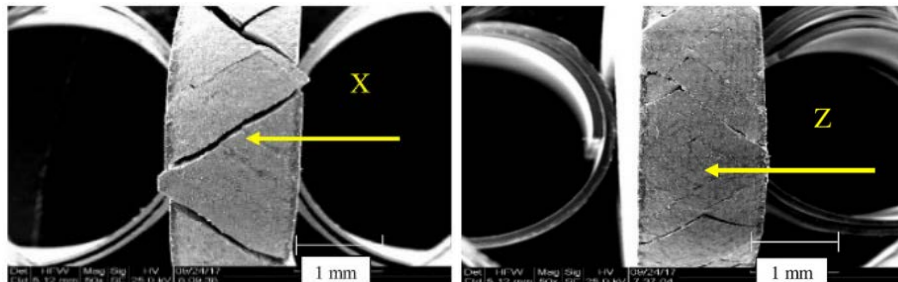


Figure 14: Circumferential fracture surface of an AlSi10Mg SHPB sample from (a) the present study and from (b) a similar study [32]

Adiabatic shear banding (ASB) is another phenomenon observed in aluminum alloys [13] due to a positive feedback loop between excessive localized shear deformation and adiabatic heating. While possibly not the dominant failure mechanism in this case, the alignment of the less homogeneous build layers with the loading axis could offer enhanced sites for localized shear banding without causing complete fracture. Scanning Electron Microscope (SEM) imaging could be used on cross sections of tested specimen to identify ASB specific abnormalities or interior delamination.

3.1.2. Charpy V-notch

Absorbed energy results obtained during the Charpy V-notch testing are presented in this section; each value is an average from between three and five repeat tests, unless otherwise noted. They are separated by processing parameters and build orientation. Values for typical cast AlSi10Mg are included as a referenced from another study of this material [30]. A comparison of both build angle and GED is shown graphically in Figure 15. More focused charts are available in Appendix A: Complete Graphical Data and other data not addressed in this section, but required by ASTM E23 can be found in Appendix B: Background Charpy Information.

Table VIII: Average AlSi10Mg Charpy v-notch absorbed energy results

	0 Degree	30 Degree	45 Degree	60 Degree	90 Degree
Low GED	3.85 ± 0.00	3.40 ± 0.02	3.02 ± 0.00	2.41 ± 0.05	2.10 ± 0.09
Med GED	5.58 ± 0.05	4.71 ± 0.14	4.10 ± 0.14	3.27 ± 0.05	2.50 ± 0.11
High GED	3.25 ± 0.12	2.84 ± 0.07	(No Data)	2.43 ± 0.10	2.19 ± 0.17

Uncertainties on the averages in Table VIII are the standard deviation based on the sample size available. It is also of note that no 45° samples were produced using the high GED due to a change in experimental setup between manufacturing runs. One of the 45°, low GED samples had errant geometry from machining error and could not be tested so that sample size was reduced to two.

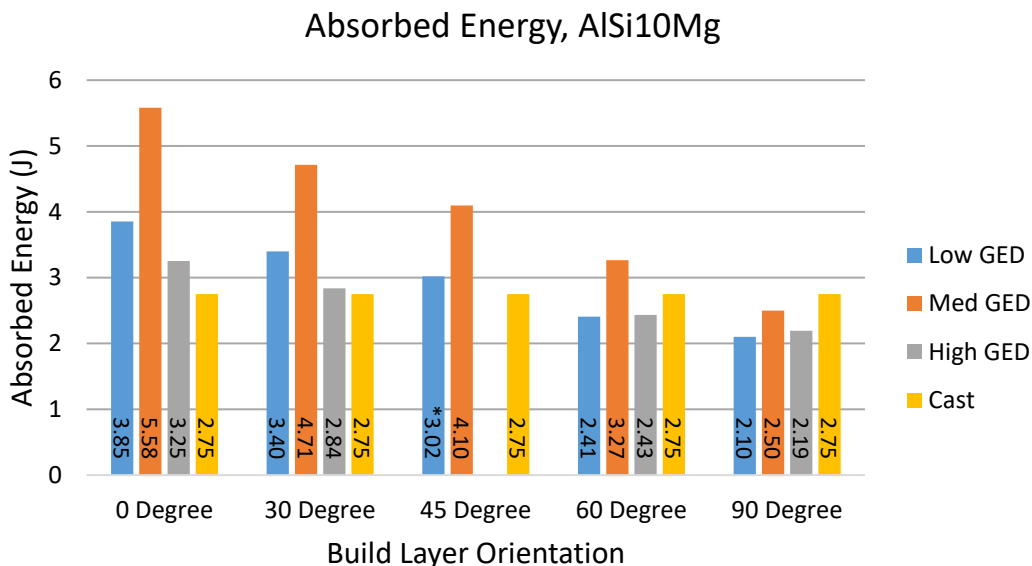


Figure 15: Average absorbed energy of aluminum Charpy v-notch specimen (*only two specimens available for testing)

The most prominent trend is the linear decrease in breaking energy from 0° to 90° for all GEDs. Linear regression of the flow stress with respect to build angle for each GED set yields R^2 values over 97%. This shows a definitive trend and implies the interlaminar boundaries are more conducive to crack initiation and propagation. Similarly, quasi static tensile results from other work indicate a reduced percent elongation when the build layers are perpendicular to the loading axis [33], possibly indicating a reduction of ductility along those boundaries. There is also a tendency for defects to congregate between build layers and even for porosity to slightly increase based on the increase of the build angle in slender structures [34], [38]. Porosity has been noted to have a negative effect on the Charpy absorbed energy performance [39], [40]. The convergence of all three GEDs with the alignment of build layer with crack propagation direction indicates that interlaminar characteristics are not greatly affected by the parameters that were varied in this study.

The variation with GED change is a considerable factor as well. Unlike the SHPB results, the medium GED parameters produced the highest Charpy impact strength by at least 13% and at most 53% (versus the lowest strength 3D printed material at each orientation). This trend is not unexpected as a parallel study has found that the GED of 45.4 J/mm^3 (medium) provides a favorable balance of microstructure and porosity [33]. GED dependent porosity can be caused by insufficient energy input leaving keyhole pores of non-melted feedstock or excessive heat accumulation allowing hydrogen diffusion within the melt. Both types can cause a reduction in Charpy breaking energy, but not necessarily in the dynamic compressive strength.

3.2. 316L

3.2.1. SHPB

SHPB flow stress data for 316L specimen was collected in an identical manner as the aluminum data. Similarly, the complete set of stress strain response plots are available in Appendix A: Complete Graphical Data. All uncertainties reported are the standard deviation of the sample set.

3.2.1.1. Processing Parameter

The three processing parameter set variations used to produce samples with relatively low, medium and high GEDs are listed in Table IV in the Experimental Methods section of this report. Flow stress results from each sample at 0° and 90° orientations and varying strain rates are presented numerically in Table IX and Table X as well as graphically in Figure 16.

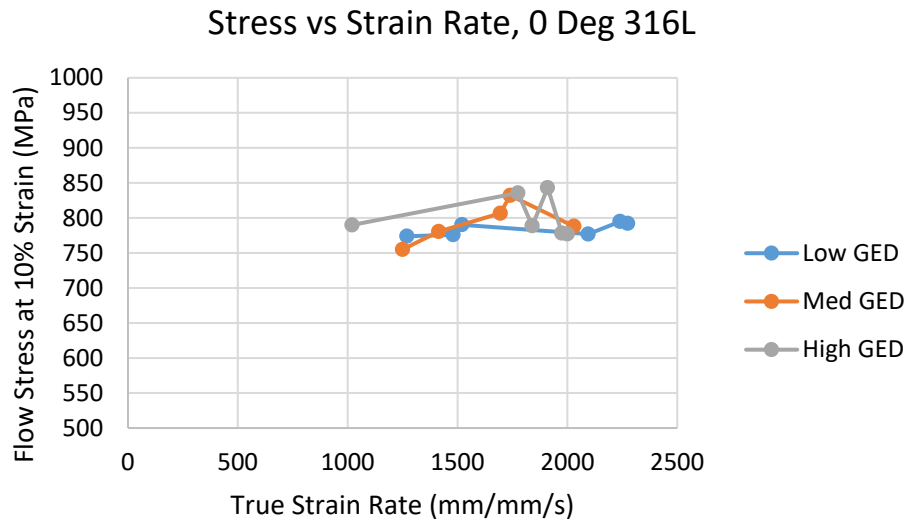
Table IX: Strain rate and flow stress results for 0° oriented 316L

Low GED		Med GED		High GED	
Strain Rate	Flow Stress	Strain Rate	Flow Stress	Strain Rate	Flow Stress
1270	774	1250	755	1020	790
1480	776	1415	780	1775	836
1520	790	1695	807	1840	789
2095	777	1740	832	1910	843
2240	795	2030	788	1975	778
2275	792			2000	777

Table X: Strain rate and flow stress results for 90° oriented 316L

Low GED		Med GED		High GED	
Strain Rate	Flow Stress	Strain Rate	Flow Stress	Strain Rate	Flow Stress
690	778	1025	817	1040	829
1145	850	1330	798	1550	822
1520	837	1595	855	1810	811
1880	789	1700	836		
1985	885	1820	803		
		2085	835		

(a)



(b)

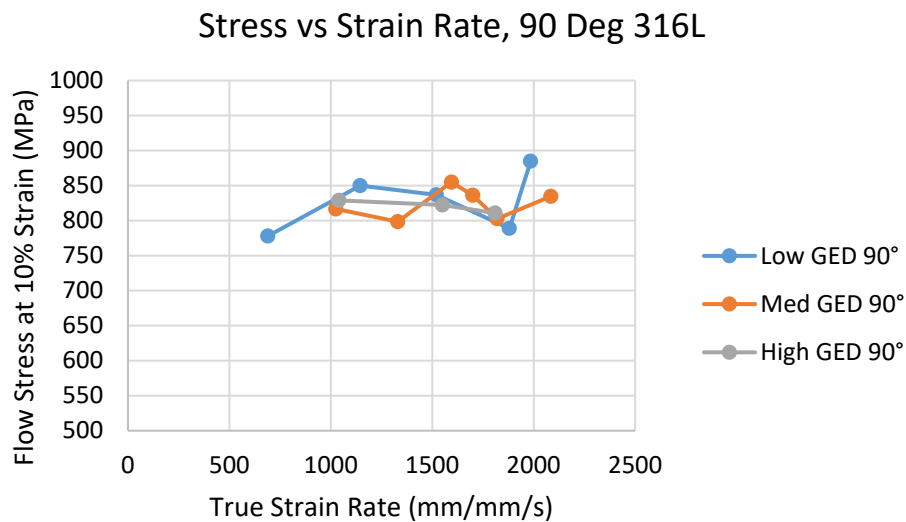


Figure 16: Relationship between flow stress and strain rate for (a) 0° and (b) 90° 316L samples

For the strain rate range tested (~700/s to 2200/s) there was no significant trend between strain rate and flow stress as shown by the scatter plots in Figure 16. Overlap of data from each set of parameters shows significantly less stratification than the aluminum samples, with the steel response appearing not to have any significant dependence on GED parameters.

The stress strain response of a representative sample from each parameter set is shown in Figure 17.

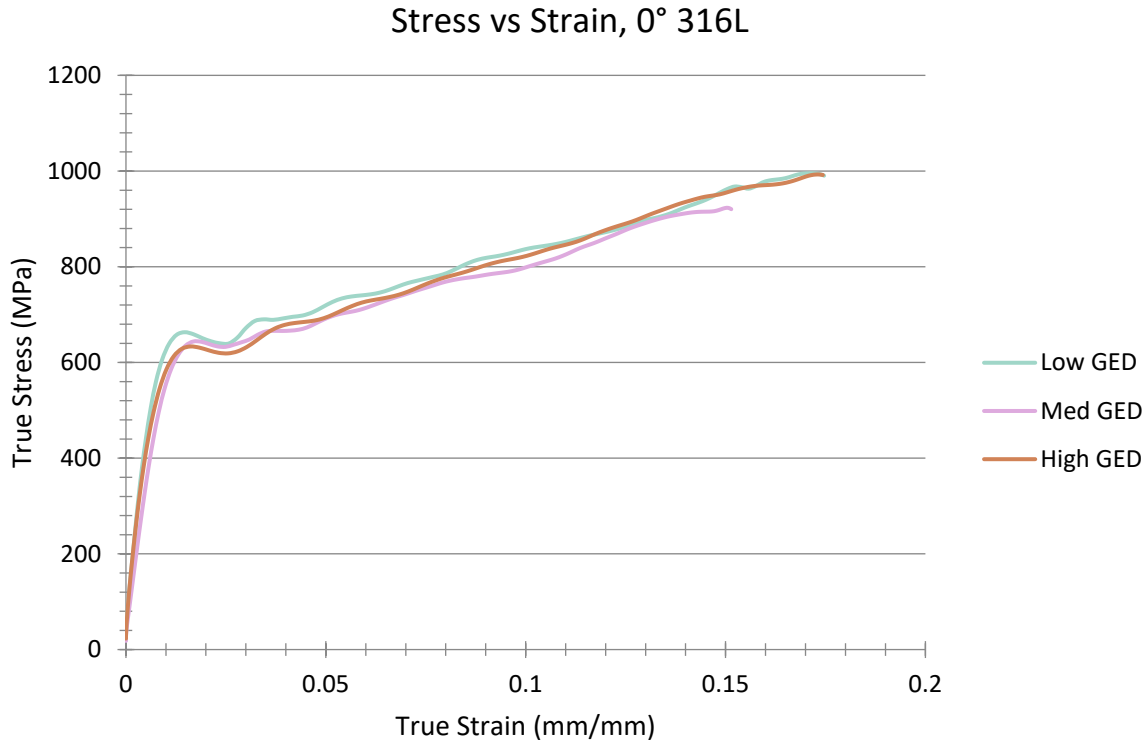
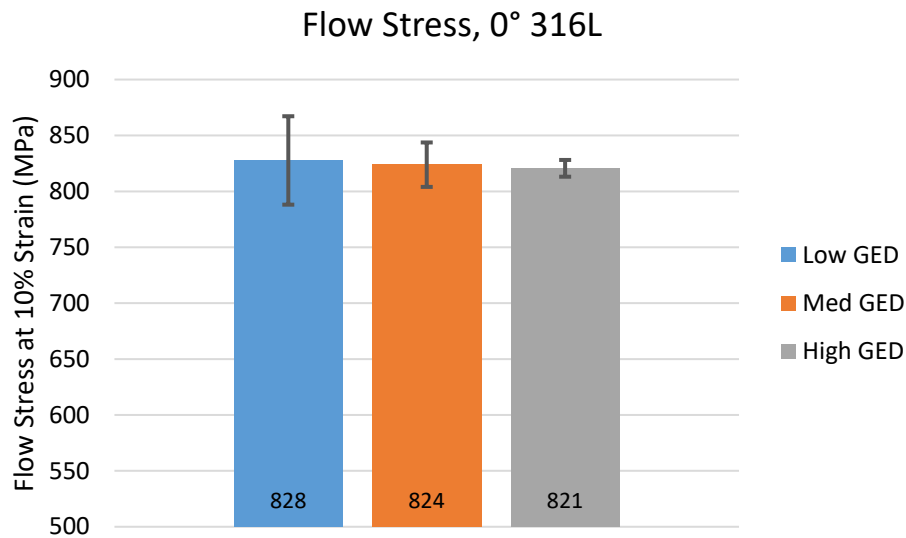


Figure 17: Representative stress strain response of 316L samples at $1.5 \times 10^3/s$ strain rate

Noticeably, the stress strain response demonstrated in Figure 17 indicates significant strain hardening over the deformation range of 3% to 18%. Samples subject to further deformation maintain the same upward slope until unloading occurs for all build angles. Due to limitations of the equipment, excessive strains and failure were unable to be reached. No sample tested was subject to catastrophic failure therefore all stress strain plots end due to separation of the sample from the bars and not due to failure. Experiments on smaller specimen can provide insight to the dominance of deformation mechanisms at further strains as the work hardening and thermal softening compete up to the point of failure.

Averages for the flow stress results of each processing parameter set at 0° and 90° are displayed in Figure 18.

(a)



(b)

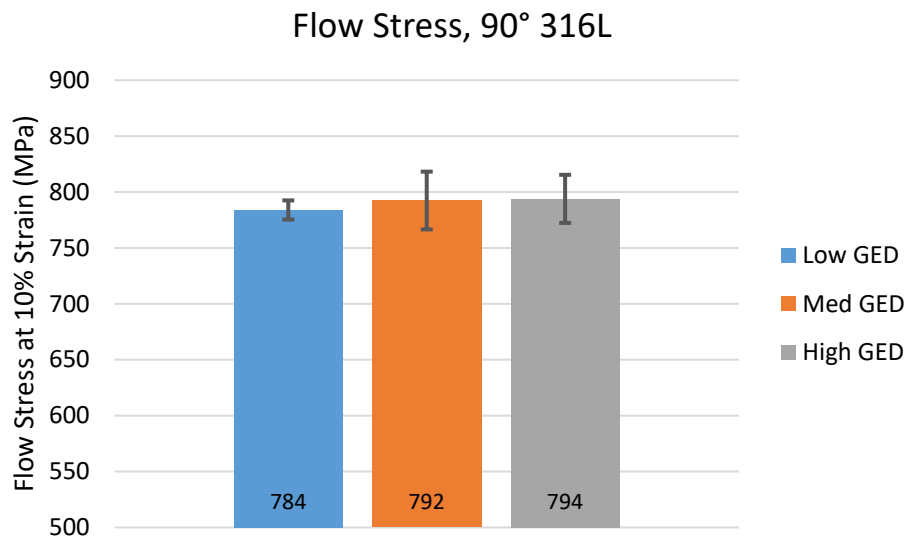


Figure 18: Average flow stress of samples from each set of processing parameters for (a) 0° and (b) 90° build orientations

The flow stress differentiation between processing parameters is very small for both 0° and 90° build layer orientations. Large overlap of the data spread also indicates little to no statistically significant difference. Figure 18 does, however, highlight the unexpected downward

trend in flow stress from the 0° to 90° build angle. This opposes to the trend seen in the AlSi10Mg samples and indicates the interlaminar characteristics don't necessarily represent a weak point for the AM 316L as they do in AlSi10Mg.

3.2.1.2. Build Angle

Results from each sample set are averaged and organized in Table XI with uncertainties listed and in displayed visually Figure 19. Samples were unavailable at the 45° build angle for high GED parameters.

Table XI: Average flow stress at 10% strain for each set of build parameters and orientations

	Low GED	Med GED	High GED
Build Angle	Flow Stress (MPa)	Flow Stress (MPa)	Flow Stress (MPa)
0 Degree	824 ± 44.21	824 ± 21.78	821 ± 09.18
30 Degree	790 ± 12.05	809 ± 25.51	807 ± 24.22
45 Degree	746 ± 39.01	817 ± 12.34	(No Data)
60 Degree	811 ± 21.20	795 ± 09.75	796 ± 19.52
90 Degree	784 ± 09.40	792 ± 28.89	783 ± 34.16

The uncertainty in these sample sets is somewhat larger than that found during aluminum testing, although the mean values have increased greatly as well. The coefficient of variation value, which compensates for changing mean, also shows a jump in the error between the AlSi10Mg and 316L samples. These values for the aluminum tests range mostly from 1-2%, the steel coefficient of variation values range mostly from 2-4% with several sets exceeding 5%. Causes for this error increase could be due to less consistent product or from machine error due to higher impact velocities required to achieve similar strain rates in the steel samples.

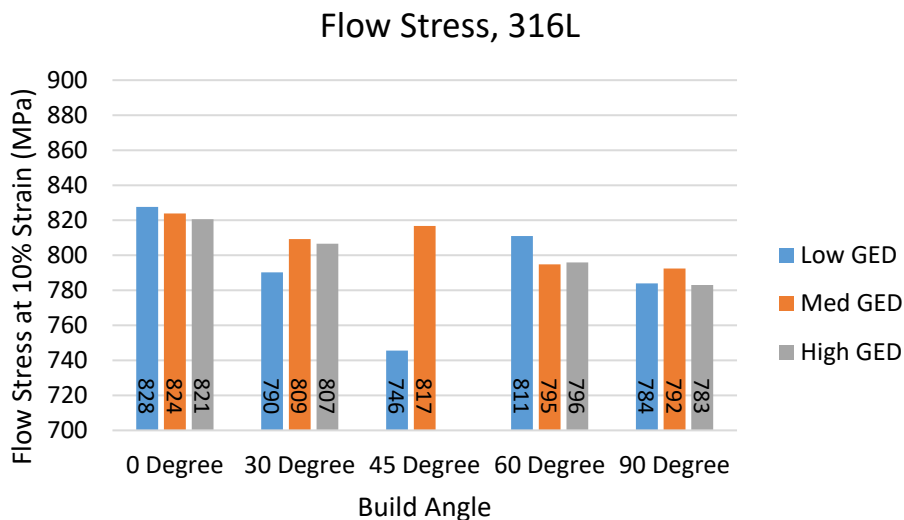


Figure 19: Average flow stress for each set of processing parameters across all build orientations

The overall downward trend of flow stress with the increase of build angle is not expected based on behavior of AM AlSi10Mg. This could indicate that molten pool boundaries (MPB), the fusion area between adjacent laser paths, creates a weaker bond than the build layer boundaries.

The low GED 45° sample set shows the largest inconsistency relative to adjacent data. This could stem from abnormal biased data scatter given the relatively large coefficient of variation (5.23%). It could also be the result of areas of poor fusion aligned along the 45° plane causing a large decrease in strength in the plane with the largest stresses experienced during compressive loading due to ductile deformation and adiabatic shear band formation.

Total reduction in flow stress from 0° to 90° was around 5% for all categories. This seems to indicate a trend for the materials, but the variance of the data is not well explained by the change in build angle. However, there may be a more meaningful relationship between them in other strain rate regimes not tested here as it has been found build layer orientation dependence can vary between quasi static, high and very high strain rate tests [32].

3.2.1.3. Temperature

As an important part of a constitutive model, temperature variation was explored briefly to establish the trend. The low end of temperature range was approximately 20°C (ambient) and elevated temperatures reached 300°C. All samples tested were of the 90° build angle from the high GED set.

Table XII: Flow stress values for 316L elevated temperature tests

	20°C	100°C	200°C	300°C
High GED, 90° Build	777 MPa	765 MPa	674 MPa	621 MPa

The flow stress reduction with increase in temperature from 20°C to 300° is just over 30%. Loss of strength is expected as the increase in temperature softens the material and increases the ductile dominance in material behavior. The varying change between the temperature levels is irregular though. Despite the regular increase in temperature of around +100°C, the flow stress drop starts small, increases 10 fold and then halves for the last interval. The temperature coefficient of the Johnson-Cook constitutive model would predict that the flow stress variation due to temperature would be constantly increasing or decreasing based on the material properties as shown in equation (10).

$$\sigma_y \propto 1 - \left[\frac{T - T_0}{T_m - T_0} \right]^m \quad (10)$$

where σ_y is the dynamic yield stress, T is the test temperature, T_m is the melting point of the material, T_0 is a reference temperature and m is the temperature parameter of the material model. The sample size for this data is then likely too small to make a meaningful model from, but the general response appears promising.

3.2.2. Charpy V-notch

Charpy v-notch absorbed energy values were found for sample sets covering each set of processing parameters at each build angle. Sample sets contained three to five specimen and the data presented in Table XIII and Figure 20 represent the average for the entire set. Data for each set is presented individually with error bars demonstrating the standard deviation in Appendix A: Complete Graphical Data.

Table XIII: 316L Charpy v-notch absorbed energy results

	0 Degree	30 Degree	45 Degree	60 Degree	90 Degree
Low GED	84.2 ± 6.6	87.6 ± 2.7	75.4 ± 1.1	82.8 ± 2.3	76.0 ± 4.0
Med GED	165.0 ± 12.5	161.9 ± 6.4	194.2 ± 1.2	185.5 ± 5.3	216.0 ± 8.6
High GED	172.3 ± 6.5	168.3 ± 0.7	183.7 ± 14.0	190.8 ± 23.8	212.5 ± 15.0

The uncertainties in Table XIII represent the standard deviation of the sample sets. From the numerical presentation of this data it is apparent that the samples produced with medium and high GEDs have a significant impact strength advantage over the low GED samples. Similar to the SHPB results, the greatest uncertainty came from the high GED parameter set.

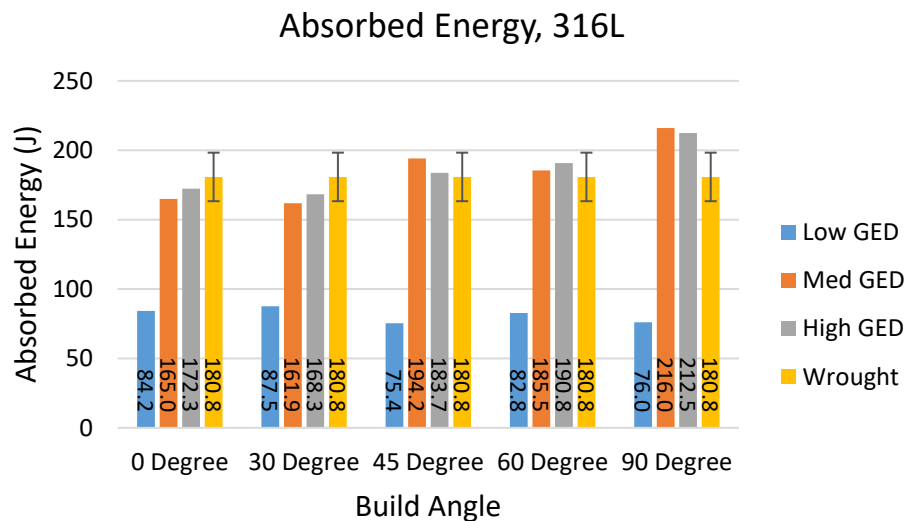


Figure 20: Average absorbed energy of stainless steel Charpy v-notch specimen

The added wrought data are from this work as well and serve as a reference of material performance to traditionally manufactured 316L. Across all build angles the medium and high GED parameters produce comparable impact strength and at 90° offer a slight advantage over wrought material. Graphical representation makes it clear that the Charpy determined impact strength of the low GED material is less than half of the medium GED, high GED and wrought samples. A study of quasi static properties and fractography on samples produced simultaneously found that the low GED (83.3 J/mm^3) was not adequate to create satisfactory fusion between build layers or melt tracks [24]. The high volume of defects due to insufficient fusion likely created low resistance pathways for crack propagation lowering the absorbed energy and returning less predictable results with respect to build angle. The higher energy densities also demonstrated considerably greater ductility, an important factor in Charpy performance, as shown in Figure 21.

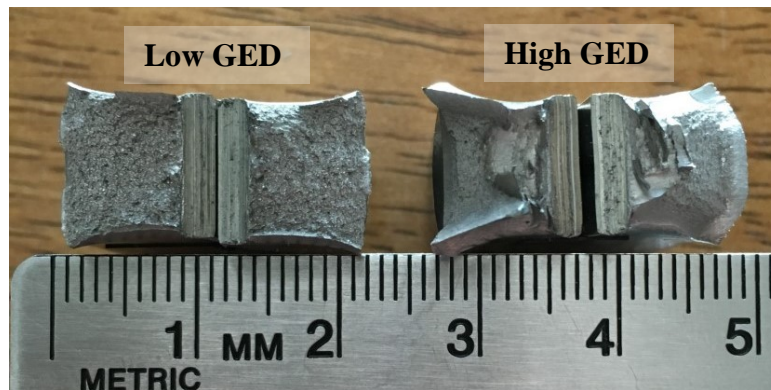


Figure 21: Fracture surface comparison between high and low GED Charpy specimen

Contrary to the adjacent studies, however, the strength appears to increase with the build angle. Quasi static testing would indicate that when the tensile stress plane is parallel to the build layers that delamination becomes more likely [34], thereby lowering the strength. Results from this work on the AlSi10Mg aluminum alloy also follow that trend, increasing in Charpy strength with declining build angle. Therefore it is possible that the interlaminar boundary behavior is

complicated by residual stresses due to extreme temperature differentials between the melt and substrate during solidification [41]. A pinning effect could also be exacerbated in the 90° orientation due to higher densities of nano-scale structure formation observed in SLM 316L [42].

4. Conclusions

The processing parameters and build layer orientation have a noticeable effect on the mechanical behavior of both AlSi10Mg and 316L, under dynamic loading conditions. The magnitude and direction of the trends varies by material and testing type.

4.1. AlSi10Mg

Split-Hopkinson pressure bar results for the AM aluminum showed a marked increase in flow stress for the low GED parameters (37.1 J/mm^3) due to improved microstructure from the higher cooling rates involved. Variation in the build angle yielded an increase in flow stress directly related to the orthogonality of the build layers and loading axis.

Maximum Charpy absorbed energy values were achieved with the medium GED parameters (45.4 J/mm^3). The moderate microstructure and reduced porosity help discourage crack propagation. The decrement of strength with the increase in build angle occurs as defects tend to concentrate on the build layer boundaries. In general, the performance is comparable to cast material as the AM absorbed energy values ranges from considerably greater to slightly below the cast values.

4.2. 316L

For SHPB tested 316L, the variation between GEDs was insignificant to draw any conclusions, although the 45° set at low GED (83.3 J/mm^3) parameters produced significantly lower flow stress than any other group. Overall the performance of 0° oriented samples was greater than that of the 90° specimen, but the intermediate data is too inconsistent to establish a correlation of flow stress with build angle. Temperature variation showed general trend, but not a significant number of samples were tested to create a model.

Results for the Charpy tests of 316L indicate the medium GED ($100. \text{ J/mm}^3$) parameters perform the best with the high GED (188 J/mm^3) close behind and ranging from 5-9% below wrought values up to 17-19% above wrought values at 0° and 90° respectively. The low GED (83.3 J/mm^3) parameters performed significantly worse, having absorbed energy values less than half of any other sample set.

4.3. Future Work

- Analysis of SHPB specimen using SEM and micro CT imaging to identify deformation mechanisms and interior failure e.g. adiabatic shear bands or minor delamination.
- Acquisition of smaller test specimen for higher strain rate testing and achieving higher strains without undue wear on the SHPB tester.
- Quasi static compressive testing in addition to further SHPB testing at significantly higher strain rates (close to 10^4) to establish statistically significant strain rate sensitivity trends.
- Verify performance of Inconel pressure bar setup for testing of higher test temperatures.
- Explore the validity of a constitutive model, such as the Johnson-Cook, in predicting the flow stress behavior of these additively manufactured materials.
- Focus on higher performing GED parameters and isolate specific variables (e.g. laser speed) for optimization.

5. References

- [1] B. E. Carroll, T. A. Palmer, and A. M. Beese, “Anisotropic tensile behavior of Ti-6Al-4V components fabricated with directed energy deposition additive manufacturing,” *Acta Mater.*, vol. 87, pp. 309–320, 2015.
- [2] L. Hirt, A. Reiser, R. Spolenak, and T. Zambelli, “Additive Manufacturing of Metal Structures at the Micrometer Scale,” *Adv. Mater.*, vol. 29, no. 17, 2017.
- [3] L. E. Murr *et al.*, “• Invited Review Metal Fabrication by Additive Manufacturing Using Laser and Electron Beam Melting Technologies,” 2012.
- [4] S. Grinde, “TOPOLOGY OPTIMIZATION FOR ADDITIVE MANUFACTURING USING SIMP METHOD,” Montana Tech, 2018.
- [5] J. Kruth, B. Vandenbroucke, J. Van Vaerenbergh, and I. Naert, “Rapid Manufacturing of Dental Prostheses by means of Selective Laser Sintering/Melting,” no. 2.
- [6] L. Xue and M. U. Islam, “Laser Consolidation-A Novel One-Step Manufacturing Process for Making Net-Shape Functional Components.”
- [7] D. Ding, Z. Pan, D. Cuiuri, and H. Li, “Wire-feed additive manufacturing of metal components: technologies, developments and future interests.”
- [8] M. J. Matthews, G. Guss, S. A. Khairallah, A. M. Rubenchik, P. J. Depond, and W. E. King, “Denudation of metal powder layers in laser powder bed fusion processes,” *Acta Mater.*, vol. 114, pp. 33–42, 2016.
- [9] W. E. Frazier, “Metal additive manufacturing: A review,” *Journal of Materials Engineering and Performance*, vol. 23, no. 6. pp. 1917–1928, 2014.
- [10] P. Hanzl, M. Zetek, T. Bakša, and T. Kroupa, “The Influence of Processing Parameters on

- the Mechanical Properties of SLM Parts,” in *Procedia Engineering*, 2015, vol. 100, no. January, pp. 1405–1413.
- [11] W. W. Chen and B. Song, *Split Hopkinson (Kolsky) Bar: Design, Testing and Applications*. 2013.
- [12] R. M. Davies, “A CRITICAL STUDY OF THE HOPKINSON PRESSURE BAR.”
- [13] B. Mishra, P. Ghosal, K. S. Kumar, V. Madhu, C. Mondal, and R. Goyal, “Plastic flow behavior of 7017 and 7055 aluminum alloys under different high strain rate test methods,” *Mater. Sci. Eng. A*, vol. 612, pp. 343–353, 2014.
- [14] J. M. Krafft, A. M. Sullivan, and C. F. Tipper, “The Effect of Static and Dynamic Loading and Temperature on the Yield Stress of Iron and Mild Steel in Compression,” 1954.
- [15] Y. Wang and Z. Jiang, “Dynamic compressive behavior of selected aluminum alloy at low temperature,” *Mater. Sci. Eng. A*, vol. 553, pp. 176–180, 2012.
- [16] F. Hughes, “The high strain-rate behaviour of polymers and nanocomposites for lightweight armour applications,” Loughborough University, 2013.
- [17] *Springer Handbook of Experimental Solid Mechanics*. 2008.
- [18] L. P. Pook, *Understanding Pendulums*. Dordrecht: Springer, 2011.
- [19] and E. A. R. T. A. Siewert, M. P. Manahan, C. N. McCowan, J. M. Holt, F. J. Marsh, “CVN history.” .
- [20] “Model IT 406 Charpy Tester.” [Online]. Available: <https://www.tiniusolsen.com/list-of-products/model-it-406>. [Accessed: 01-Jan-2017].
- [21] A. S. F. T. A. MATERIALS, “ASTM E23 – 16b: Standard Test Methods for Notched Bar Impact Testing of Metallic Materials.,” *ASTM*, 2016.
- [22] E. O. Olakanmi, R. F. Cochrane, and K. W. Dalgarno, “A review on selective laser

- sintering/melting (SLS/SLM) of aluminium alloy powders: Processing, microstructure, and properties,” *J. Prog. Mater. Sci.*, vol. 74, pp. 401–477, 2015.
- [23] K. Antony, N. Arivazhagan, and K. Senthilkumaran, “Numerical and experimental investigations on laser melting of stainless steel 316L metal powders,” *J. Manuf. Process.*, vol. 16, pp. 345–355, 2014.
- [24] S. Keckler, “MATERIAL PROPERTIES OF LASER POWDER BED FUSION PROCESSED 316L STAINLESS STEEL,” Montana Tech, 2018.
- [25] Z. Sun, X. Tan, S. Beng Tor, and W. Yee Yeong, “Selective laser melting of stainless steel 316L with low porosity and high build rates,” 2016.
- [26] K. Kempen, L. Thijs, E. Yasa, M. Badrossamay, W. Verhecke°, and J.-P. Kruth, “PROCESS OPTIMIZATION AND MICROSTRUCTURAL ANALYSIS FOR SELECTIVE LASER MELTING OF AlSi10Mg.”
- [27] D. Herzog, V. Seyda, E. Wycisk, and C. Emmelmann, “Additive manufacturing of metals,” *Acta Mater.*, vol. 117, pp. 371–392, 2016.
- [28] E. Zaretsky, A. Stern, and N. Frage, “Dynamic response of AlSi10Mg alloy fabricated by selective laser melting,” *Mater. Sci. Eng. A*, vol. 688, pp. 364–370, Mar. 2017.
- [29] “EOS Aluminium AlSi10Mg,” Krailling / München, 2014.
- [30] K. Kempen, L. Thijs, J. Van Humbeeck, and J. P. Kruth, “Mechanical Properties of AlSi10Mg Produced by Selective Laser Melting,” in *Physics Procedia*, 2012.
- [31] D. Buchbinder, W. Meiners, K. Wissenbach, and R. Poprawe, “Selective laser melting of aluminum die-cast alloy-Correlations between process parameters, solidification conditions, and resulting mechanical properties,” *J. Laser Appl*, vol. 27, p. 29205, 2015.
- [32] B. Nurel, M. Nahmany, N. Frage, A. Stern, and O. Sadot, “Split Hopkinson pressure bar

- tests for investigating dynamic properties of additively manufactured AlSi10Mg alloy by selective laser melting,” *Addit. Manuf.*, vol. 22, pp. 823–833, Aug. 2018.
- [33] L. J. Suttey, “EVALUATION OF METALLURGICAL AND MECHANICAL PROPERTIES OF AlSi10Mg PRODUCED BY SELECTIVE LASER MELTING,” Montana Tech, 2018.
- [34] G. Theses and R. Penn, “Digital Commons @ Montana Tech 3D PRINTING OF 316L STAINLESS STEEL AND ITS EFFECT ON MICROSTRUCTURE AND MECHANICAL PROPERTIES,” 2017.
- [35] B. Abstetar, “SLM PROCESSING-MICROSTRUCTURE-MECHANICAL PROPERTY CORRELATION IN AN ALUMINUM ALLOY PRODUCED BY ADDITIVE MANUFACTURING,” 2016.
- [36] ASM International, “Volume 8: Mechanical Testing and Evaluation,” in *ASM Handbook*, 2000.
- [37] N. Read, W. Wang, K. Essa, and M. M. Attallah, “Selective laser melting of AlSi10Mg alloy: Process optimisation and mechanical properties development,” *Mater. Des.*, 2015.
- [38] E. Stugelmayer, “CHARACTERIZATION OF PROCESS INDUCED DEFECTS IN LASER POWDER BED FUSION PROCESSED ALSI10MG ALLOY,” 2018.
- [39] G. Terán, S. Capula-Colindres, D. Angeles-Herrera, J. C. Velázquez, and M. J. Fernández-Cueto, “Estimation of fracture toughness KIC from Charpy impact test data in T-welded connections repaired by grinding and wet welding,” *Eng. Fract. Mech.*, vol. 153, pp. 351–359, 2016.
- [40] N. Hrabe, R. White, and E. Lucon, “Effects of internal porosity and crystallographic texture on Charpy absorbed energy of electron beam melting titanium alloy (Ti-6Al-4V),”

Mater. Sci. Eng. A, 2019.

- [41] B. Song *et al.*, “Differences in microstructure and properties between selective laser melting and traditional manufacturing for fabrication of metal parts: A review,” *Front. Mech. Eng.*, vol. 10, no. 2, pp. 111–125, 2015.
- [42] Y. Zhong, L. Liu, S. Wikman, D. Cui, and Z. Shen, “Intragranular cellular segregation network structure strengthening 316L stainless steel prepared by selective laser melting,” *J. Nucl. Mater.*, 2016.

6. Appendix A: Complete Graphical Data

6.1. AlSi10Mg SHPB Graphs

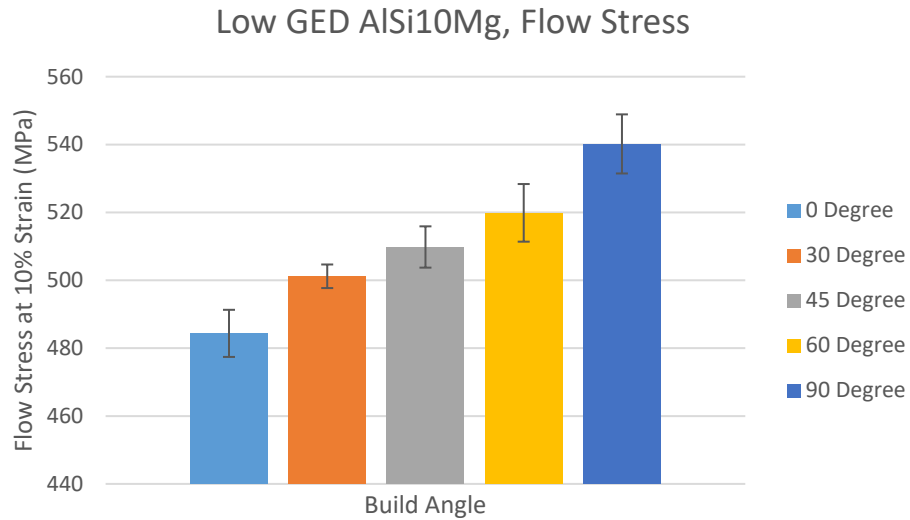


Figure 22: Average flow stress of low GED AlSi10Mg (error bars represent standard deviation)

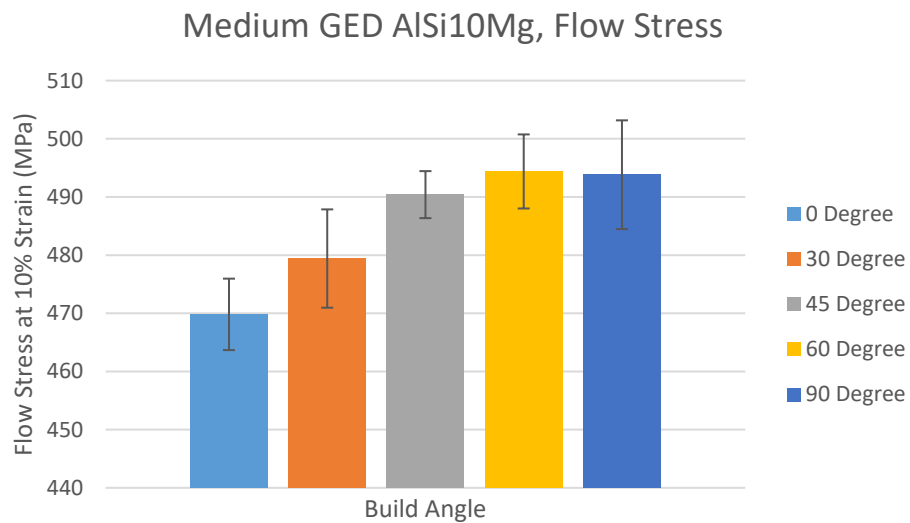


Figure 23: Average flow stress of medium GED AlSi10Mg (error bars represent standard deviation)

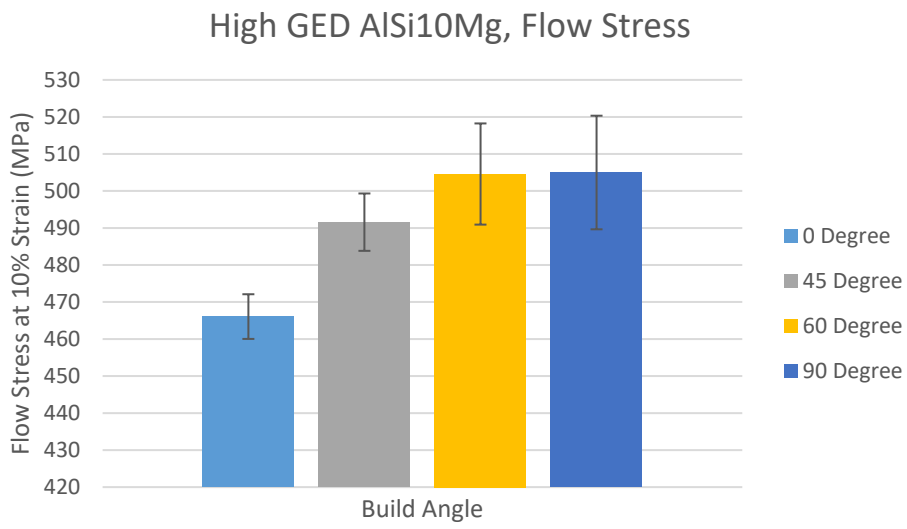


Figure 24: Average flow stress of high GED AlSi10Mg (error bars represent standard deviation)

6.2. AlSi10Mg Charpy Graphs

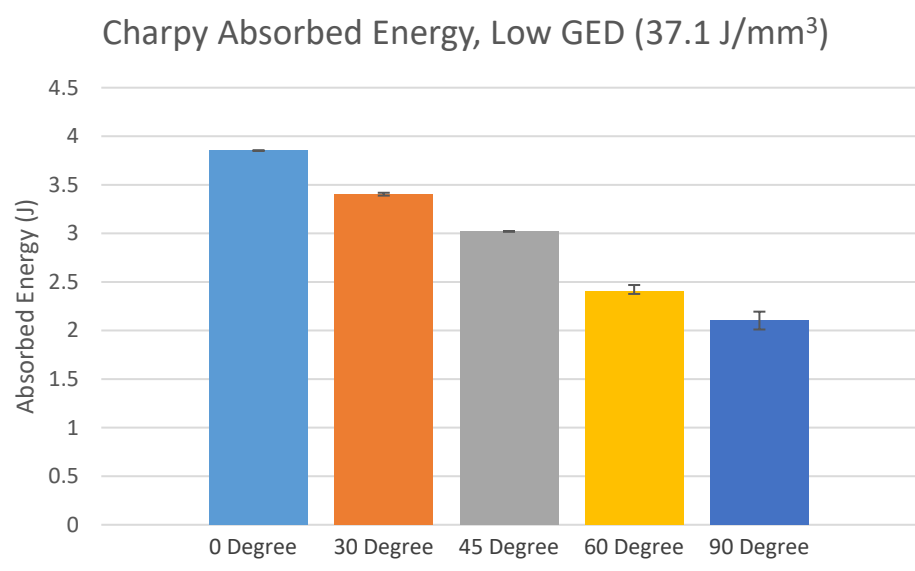


Figure 25: Average absorbed energy of low GED AlSi10Mg Charpy v-notch specimen (error bars represent standard deviation)

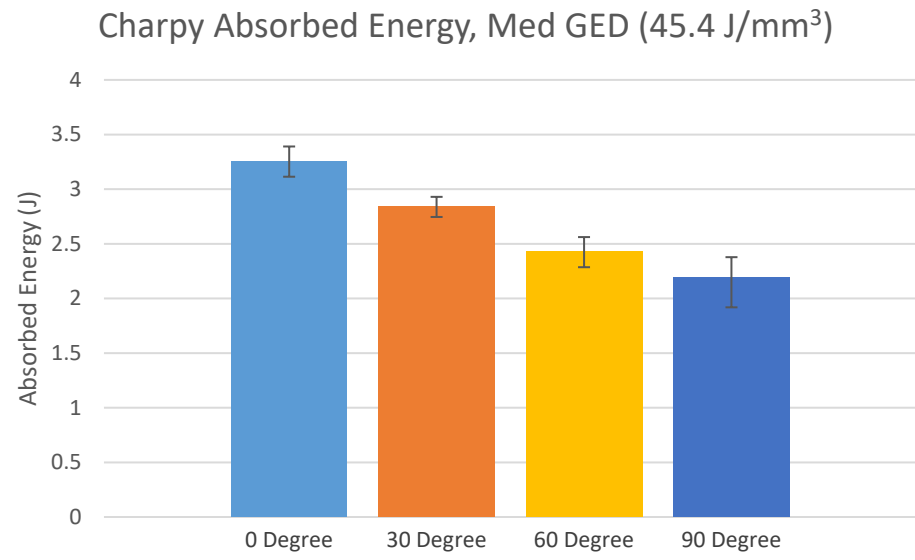


Figure 26: Average absorbed energy of medium GED AlSi10Mg Charpy v-notch specimen (error bars represent standard deviation)

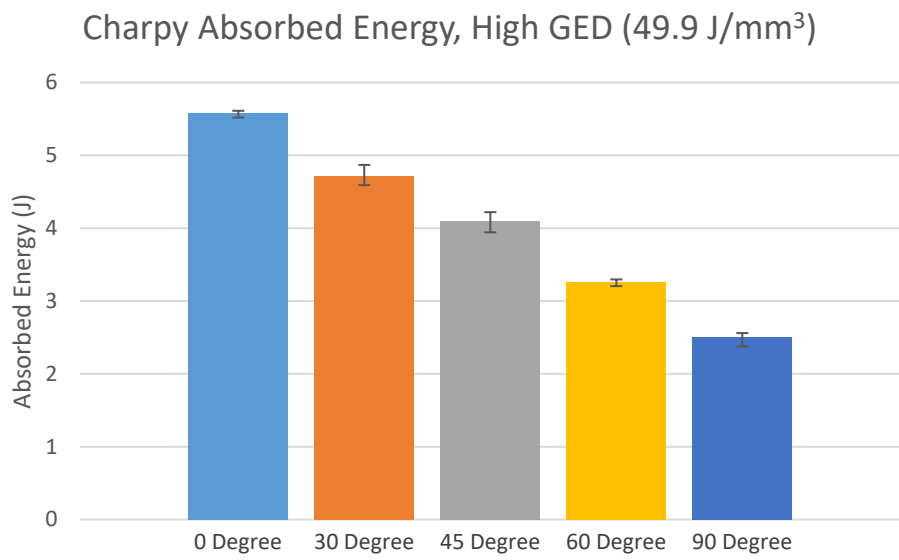


Figure 27: Average absorbed energy of high GED AlSi10Mg Charpy v-notch specimen (error bars represent standard deviation)

6.3. 316L SHPB Graphs

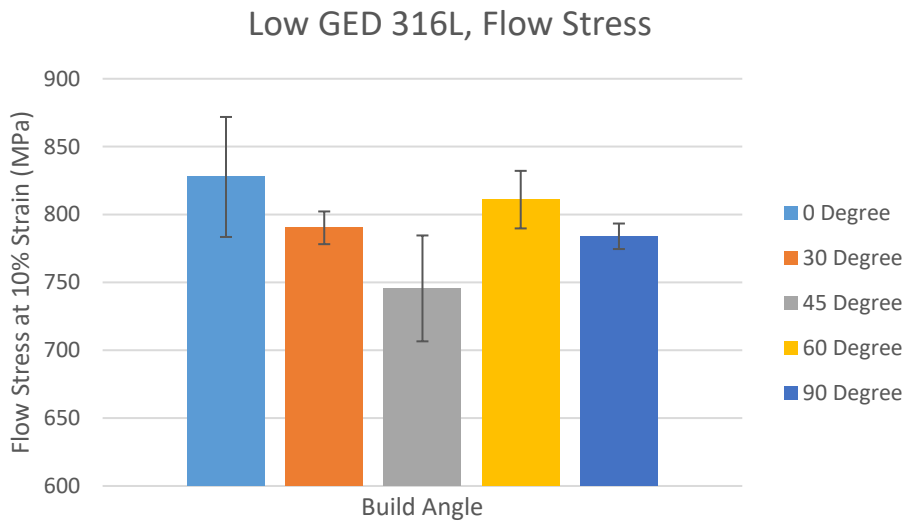


Figure 28: Average flow stress of Low GED 316L (error bars represent standard deviation)

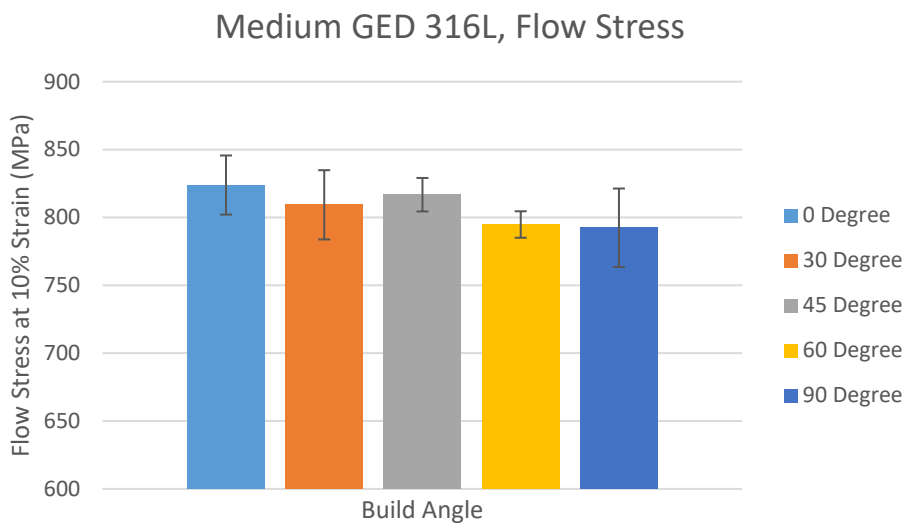


Figure 29: Average flow stress of medium GED 316L (error bars represent standard deviation)

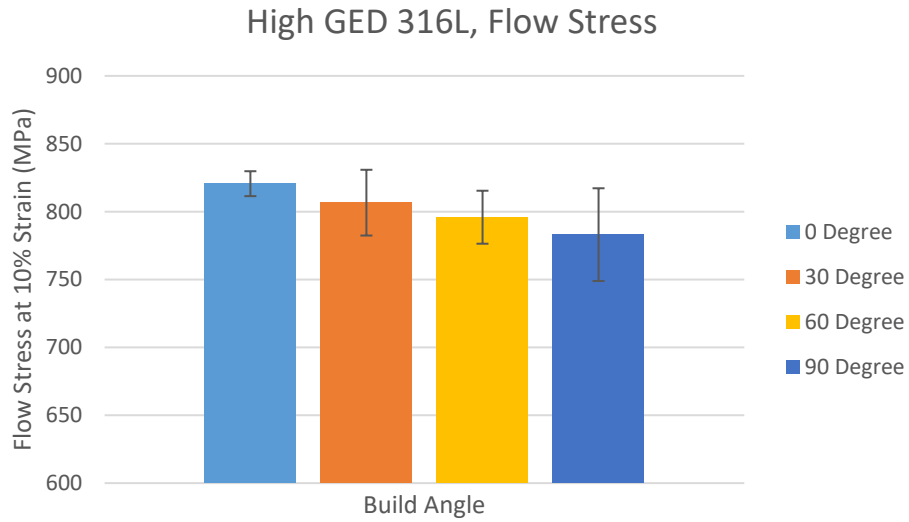


Figure 30: Average flow stress of high GED 316L (error bars represent standard deviation)

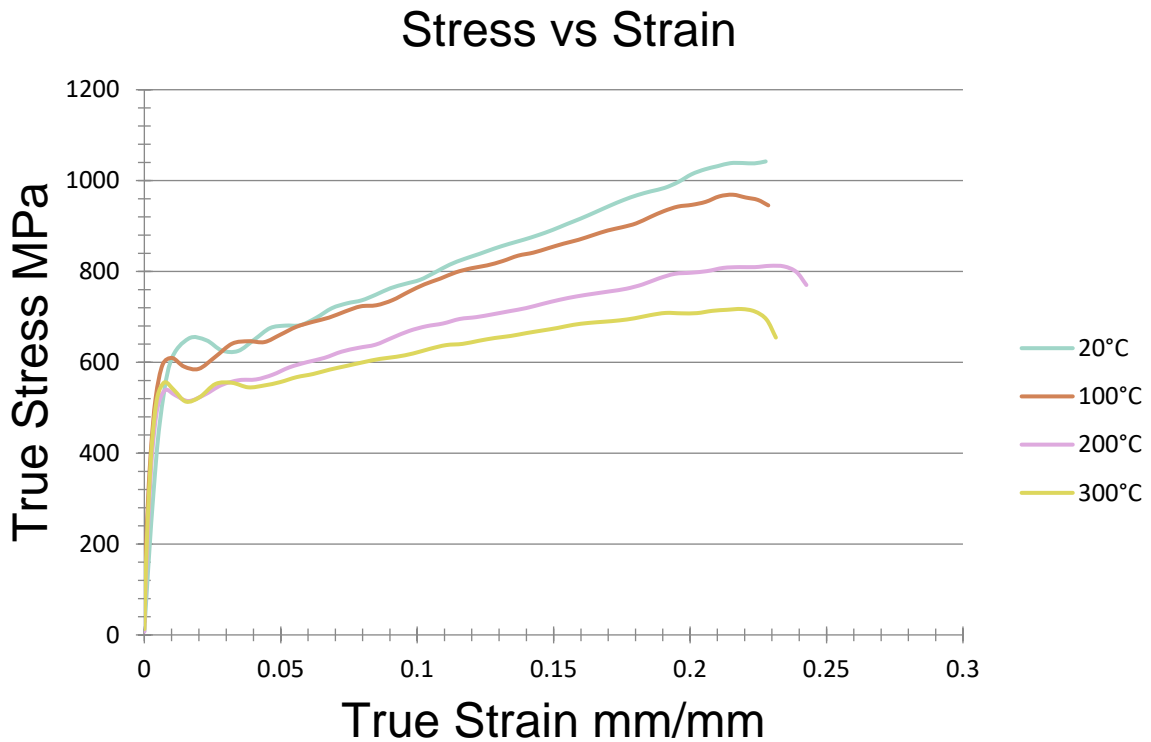


Figure 31: Stress Strain response of High GED 316L at elevated temperatures

6.4. 316L Charpy Graphs

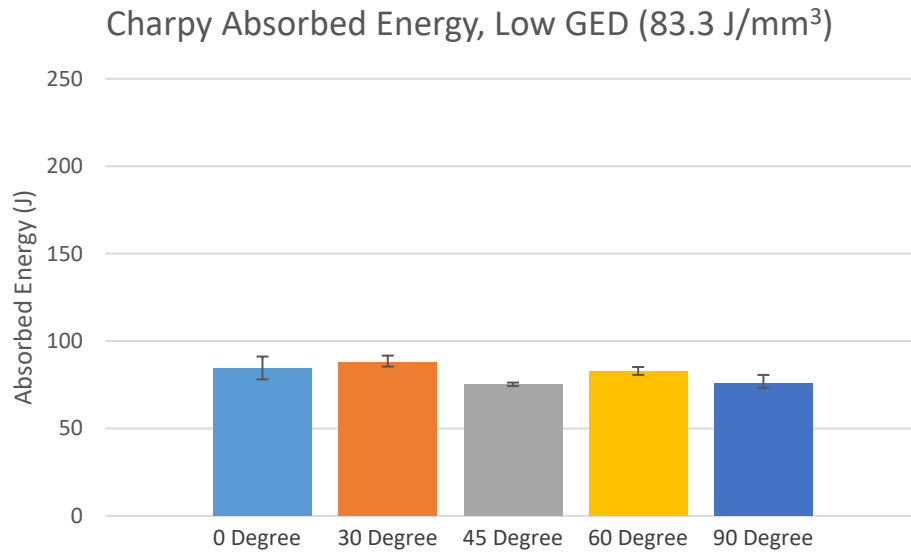


Figure 32: Average absorbed energy of low GED 316L Charpy v-notch specimen (error bars represent standard deviation)

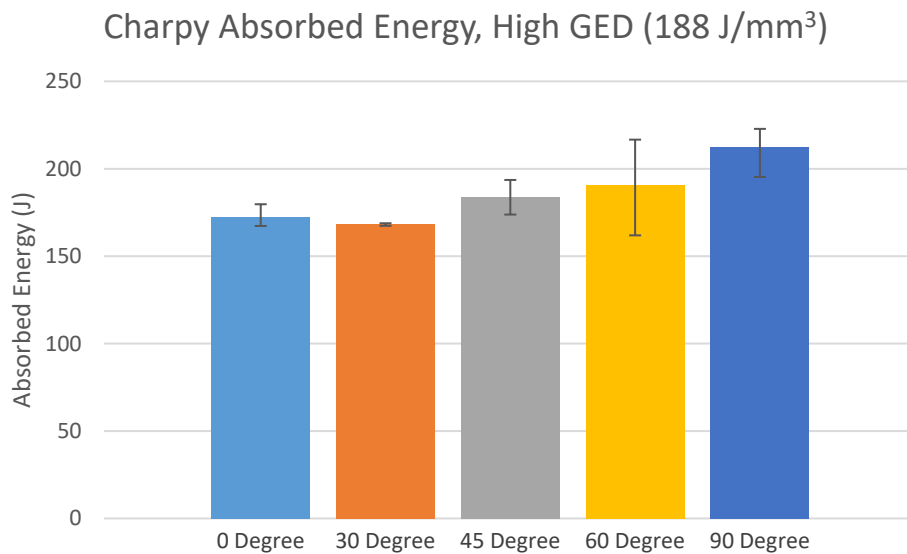


Figure 33: Average flow stress of high GED 316L (error bars represent standard deviation)

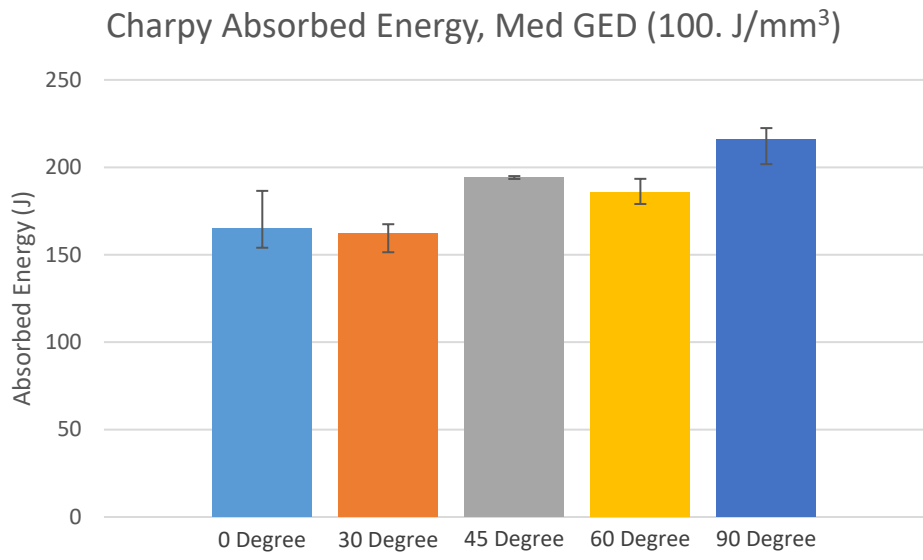


Figure 34: Average flow stress of high GED 316L (error bars represent standard deviation)

7. Appendix B: Background Charpy Information

Table XIV: Low GED AISi10Mg Charpy Information

Specimen ID	Build Angle	Breaking Energy (J)	Specimen Type	Striker Radius (mm)	Temperature (°C)
C24	0	3.8524	Charpy	8	18
C25	0	3.8524	Charpy	8	18
C26	0	3.8524	Charpy	8	18
C27	30	3.4182	Charpy	8	18
C28	30	3.3889	Charpy	8	18
C29	30	3.3889	Charpy	8	18
C30	45	No Data	Charpy	8	18
C31	45	3.0203	Charpy	8	18
C32	45	3.0203	Charpy	8	18
C33	60	2.3766	Charpy	8	18
C34	60	2.3766	Charpy	8	18
C35	60	2.4685	Charpy	8	18
C36	90	2.1941	Charpy	8	18
C37	90	2.0105	Charpy	8	18
C38	90	2.1012	Charpy	8	18

Table XV: Med GED AISi10Mg Charpy Information

Specimen ID	Build Angle	Breaking Energy (J)	Specimen Type	Striker Radius (mm)	Temperature (°C)
C39	0	5.5188	Charpy	8	18
C40	0	5.6118	Charpy	8	18
C41	0	5.6118	Charpy	8	18
C42	30	4.5906	Charpy	8	18
C43	30	4.6833	Charpy	8	18
C44	30	4.8687	Charpy	8	18
C45	45	3.9429	Charpy	8	18
C46	45	4.1278	Charpy	8	18
C47	45	4.2203	Charpy	8	18
C48	60	3.2046	Charpy	8	18
C49	60	3.2967	Charpy	8	18
C50	60	3.2967	Charpy	8	18
C51	90	2.3766	Charpy	8	18
C52	90	2.5604	Charpy	8	18
C53	90	2.5604	Charpy	8	18

Table XVI: High GED AlSi10Mg Charpy Information

Specimen ID	Build Angle	Breaking Energy (J)	Specimen Type	Striker Radius (mm)	Temperature (°C)
C1	0	3.114	Charpy	8	25
C3	0	3.2984	Charpy	8	25
C5	0	3.2062	Charpy	8	25
C7	0				
C9	0	3.3907	Charpy	8	25
C2	30	2.8377	Charpy	8	25
C4	30	2.9297	Charpy	8	25
C6	30	2.8377	Charpy	8	25
C8	30	2.8377	Charpy	8	25
C10	30	2.7456	Charpy	8	25
C13	60	2.3778	Charpy	8	25
C14	60	2.5616	Charpy	8	25
C15	60	2.2859	Charpy	8	25
C16	60	2.4697	Charpy	8	25
C17	60	2.4697	Charpy	8	25
C11	90	2.2859	Charpy	8	24
C12	90	2.1941	Charpy	8	24
C18	90	2.3778	Charpy	8	24
C19	90	2.1941	Charpy	8	24
C20	90	1.9187	Charpy	8	24

Table XVII: Low GED 316L Charpy Information

Specimen ID	Build Angle	Breaking Energy (J)	Specimen Type	Striker Radius (mm)	Temperature (°C)
C24	0	78.037	Charpy	8	20
C25	0	83.464	Charpy	8	20
C26	0	91.122	Charpy	8	20
C27	30	85.377	Charpy	8	20
C28	30	88.803	Charpy	8	20
C29	30				
C39	30	91.673	Charpy	8	20
C40	30	85.604	Charpy	8	20
C41	30	86.289	Charpy	8	20
C30	45	76.219	Charpy	8	20
C31	45	75.771	Charpy	8	20
C32	45	74.204	Charpy	8	20
C33	60	85.149	Charpy	8	20
C34	60	80.611	Charpy	8	20
C35	60	82.649	Charpy	8	20
C36	90	80.611	Charpy	8	20
C37	90	74.316	Charpy	8	20
C38	90	73.199	Charpy	8	20

Table XVIII: Medium GED 316L Charpy Information

Specimen ID	Build Angle	Breaking Energy (J)	Specimen Type	Striker Radius (mm)	Temperature (°C)
C1	0	162.88	Charpy	8	21
C2	0	162.02	Charpy	8	21
C3	0	154	Charpy	8	21
C4	0	186.53	Charpy	8	21
C5	0	159.53	Charpy	8	21
C16	30	160.29	Charpy	8	21
C17	30	164.49	Charpy	8	21
C18	30	165.85	Charpy	8	21
C19	30	167.46	Charpy	8	21
C20	30	151.42	Charpy	8	21
C21	45	193.35	Charpy	8	21
C22	45				
C23	45	194.98	Charpy	8	21
C8	60	185.27	Charpy	8	21
C9	60	193.41	Charpy	8	21
C10	60	179.03	Charpy	8	21

C11	60	183.03	Charpy	8	21
C12	60	186.53	Charpy	8	21
C6	90	214.13	Charpy	8	21
C7	90	222.44	Charpy	8	21
C13	90	220	Charpy	8	21
C14	90	221.56	Charpy	8	21
C15	90	201.82	Charpy	8	21

Table XIX: High GED 316L Charpy Information

Specimen ID	Build Angle	Breaking Energy (J)	Specimen Type	Striker Radius (mm)	Temperature (°C)
C42	0	170	Charpy	8	21
C43	0	167.27	Charpy	8	21
C44	0	179.71	Charpy	8	21
C45	30	168.72	Charpy	8	21
C46	30	168.35	Charpy	8	21
C47	30	167.35	Charpy	8	21
C57	30	168.84	Charpy	8	19
C48	45				
C49	45	173.81	Charpy	8	21
C50	45	193.61	Charpy	8	21
C51	60	196.18	Charpy	8	21
C52	60	208.74	Charpy	8	21
C53	60	216.66	Charpy	8	21
C58	60	170.7	Charpy	8	19
C59	60	161.91	Charpy	8	19
C54	90	219.43	Charpy	8	21
C55	90	222.82	Charpy	8	21
C56	90	195.3	Charpy	8	21

Table XX: Wrought 316L Charpy Information

Specimen ID	Build Angle	Breaking Energy (J)	Specimen Type	Striker Radius (mm)	Temperature (°C)
SSW-C1	N/A	172.31	Charpy	8	21
SSW-C2	N/A	200.06	Charpy	8	21
SSW-C3	N/A	199.31	Charpy	8	21
SSW-C4	N/A	164	Charpy	8	21
SSW-C5	N/A	168.33	Charpy	8	21

SIGNATURE PAGE

This is to certify that the thesis prepared by Kristofer S. Kuelper entitled "Dynamic Mechanical Response of Additively Manufactured 316L and AlSi10Mg" has been examined and approved for acceptance by the Department of General Engineering, Montana Technological University, on this 23rd day of April, 2019.



Brahmananda Pramanik, PhD, Assistant Professor
Department of General Engineering
Chair, Examination Committee



Todd Hoffman, PhD, Associate Professor
Department of Petroleum Engineering
Member, Examination Committee



K.V. Sudhakar, PhD, Professor
Department of Metallurgical and Materials Engineering
Member, Examination Committee



Steve Tarrant, MS, Assistant Professor
Department of Mechanical Engineering
Member, Examination Committee